Chiral symmetry restoration in heavy-ion collisions at intermediate energies

A. Palmese,[1] W. Cassing,[1] E. Seifert,[1] T. Steinert,[1] P. Moreau,[2] and E. L. Bratkovskaya[2,3]
[1]*Institut für Theoretische Physik, Universität Giessen, Germany*
[2]*Institute for Theoretical Physics, Johann Wolfgang Goethe Universität, Frankfurt am Main, Germany*
[3]*GSI Helmholtzzentrum für Schwerionenforschung GmbH, Darmstadt, Germany*
(Received 14 July 2016; revised manuscript received 15 September 2016; published 24 October 2016)

We study the effect of the chiral symmetry restoration (CSR) on heavy-ion collisions observables in the energy range $\sqrt{s_{NN}} = 3$–20 GeV within the parton-hadron-string dynamics (PHSD) transport approach. The PHSD includes the deconfinement phase transition as well as essential aspects of CSR in the dense and hot hadronic medium, which are incorporated in the Schwinger mechanism for the hadronic particle production. We adopt different parametrizations of the nuclear equation of state from the nonlinear σ-ω model, which enter in the computation of the quark scalar density for the CSR mechanism, in order to estimate the uncertainty in our calculations. For the pion-nucleon Σ term we adopt $\Sigma_\pi \approx 45$ MeV, which corresponds to some world average. Our systematic studies show that chiral symmetry restoration plays a crucial role in the description of heavy-ion collisions at $\sqrt{s_{NN}} = 3$–20 GeV, realizing an increase of the hadronic particle production in the strangeness sector with respect to the nonstrange one. We identify particle abundances and rapidity spectra to be suitable probes in order to extract information about CSR, while transverse mass spectra are less sensitive. Our results provide a microscopic explanation for the so-called horn structure in the excitation function of the K^+/π^+ ratio: The CSR in the hadronic phase produces the steep increase of this particle ratio up to $\sqrt{s_{NN}} \approx 7$ GeV, while the drop at higher energies is associated to the appearance of a deconfined partonic medium. Furthermore, the appearance and disappearance of the horn-structure are investigated as functions of the system size and collision centrality. We close this work by an analysis of strangeness production in the (T,μ_B) plane (as extracted from the PHSD for central Au+Au collisions) and discuss the possibilities to identify a possible critical point in the phase diagram.

DOI: 10.1103/PhysRevC.94.044912

I. INTRODUCTION

The main goal of heavy-ion collision (HIC) physics is the study of the behavior of nuclear matter at high temperatures and/or high densities. In particular, the major interest is the investigation of the nuclear-matter phase diagram as a function of temperature and baryon chemical potential. According to quantum-chromodynamics (QCD), at large temperatures and densities the hadrons cannot survive anymore as bound states and they dissolve, forming the so-called quark-gluon plasma (QGP). At Relativistic Heavy-Ion Collider (RHIC) energies the creation of a QGP, identified as an almost perfect fluid [1] has been proven experimentally for the first time. Actually, the properties of this deconfined state of matter are still debated, as well as the phase boundaries to the hadronic phase. In order to shed some light on this issue, many heavy-ion experiments have been performed at the Super-Proton Synchrotron (SPS), RHIC, and the Large Hadron Collider (LHC) and will be performed in the future at the Facility for Antiproton and Ion Research (FAIR) as well as the Nuclotron-Based Ion Collider Facility (NICA). The crucial challenge is to identify in the final particle distributions those signatures which allow us to disentangle the QGP contribution, which is impossible to observe directly or independently.

The strange particle production has always been suggested as one of the most sensitive observables that could indicate the creation of a QGP during the early stages of a HIC. The earliest suggested signature is the strangeness enhancement in $A + A$ collisions with respect to elementary $p + p$ collisions [2,3]. Gazdzicki and Gorenstein [4] proposed that a sharp rise and drop in the excitation function of the K^+/π^+ ratio (so-called horn) should show up due to the appearance of a QGP phase at a center-of-mass energy $\sqrt{s_{NN}} \sim 7$ GeV.[1] Several statistical models [5–7] have succeeded in reproducing the trend of the experimental observation of the K^+/π^+ ratio and other strange to nonstrange particle ratios, but they can provide only a statistical description of the heavy-ion collision process. On the other hand there was no conclusive interpretation of the horn from dynamical approaches for HIC, like microscopic transport models [8–10]. Only recently, the parton-hadron-string dynamics (PHSD), a transport approach describing HIC on the basis of partonic, hadronic, and string degrees of freedom, obtained a striking improvement on this issue when including chiral symmetry restoration (CSR) in the string decay for hadronic particle production [11]. Within the PHSD approach it has been suggested that the horn feature emerges in the energy dependence of the K^+/π^+ ratio, both due to CSR, which is responsible for the rise at low energies, and to the appearance of a deconfined partonic medium at higher energies, which is responsible for the drop at top SPS energies.

Apart from deconfinement, the chiral symmetry restoration addresses another aspect of the QCD phase diagram in the (T,μ_B) plane as an additional transition between a phase with broken and a phase with restored chiral symmetry. As in case of the QCD deconfinement phase transition, the

[1]In this work we adopt natural units; hence $\hbar = c = 1$.

boundaries of the CSR phase transition line are not well known. Lattice QCD (lQCD) calculations show that at vanishing baryon chemical potential $\mu_B = 0$ the CSR takes place at roughly the same critical temperature and energy density as the deconfinement phase transition, which is a crossover. At finite baryon chemical potential lQCD calculations cannot be performed due to the sign problem and one must rely on effective models (or extrapolations) in order to study the QCD phase transitions [12–16]. Different models support the idea that at finite chemical potential a partially restored phase is achieved before the deconfinement occurs [17–19]. In order to distinguish the two phases of such a transition, effective models use the scalar quark condensate $\langle \bar{q}q \rangle$ as an order parameter. As the baryon density and temperature increase, the scalar quark condensate $\langle \bar{q}q \rangle$ is expected to decrease from a nonvanishing value in the vacuum to $\langle \bar{q}q \rangle \approx 0$ which corresponds to CSR. Since $\langle \bar{q}q \rangle$ is not a measurable quantity, it is crucial to determine experimental observables which are sensitive to this feature. Dilepton spectroscopy has been in the focus in this respect since in a chirally restored phase the spectral functions of the ρ and a_1 mesons should become identical. However, no clear evidence has been achieved so far [20]. On the other hand, the strangeness production at alternating-gradient synchrotron (AGS) and lower SPS energies was suggested to be a signature of CSR [11].

In this work we will extend the analysis in Ref. [11] and perform a systematic study within the PHSD approach on effects of the CSR on final particle distributions in HICs in the energy range $\sqrt{s_{NN}} = 3$–20 GeV. The PHSD is particularly suited to this aim since it includes both hadronic and partonic degrees of freedom [21] and has been extensively used to describe HIC observables from SPS to LHC energies [22–24].

This study is organized as follows: In Sec. II we briefly recall the basic ingredients of the PHSD approach, while in Sec. III we illustrate the string fragmentation included in PHSD and the most recent extension of this particle production mechanism to incorporate essential aspects of chiral symmetry restoration. Whereas in Ref. [11] the focus has been on the effects of CSR and in particular of the partonic phase, we here also discuss the sensitivity of our results on different parameter settings for the nuclear equation of state (EoS) within the nonlinear σ-ω model and examine the role of three-meson channels for strangeness production ($3M \leftrightarrow B\bar{B}$). In Sec. IV we present the calculated results from PHSD—with and without the inclusion of CSR—for the particle rapidity spectra incorporating different nuclear equations of state in order to investigate the uncertainties of our approach. In addition to Ref. [11] we evaluate the transverse mass spectra for protons, pions, kaons, and antikaons from central collisions of heavy systems in the energy range from 2 to 158 A GeV with a special focus on the strange particle production. The excitation functions for the ratios K^+/π^+, K^-/π^-, and $(\Lambda + \Sigma^0)/\pi$, together with their uncertainties, complete Sec. IV, where a comparison with experimental data is performed wherever possible. In Sec. V we explore further new aspects of CSR in heavy-ion collisions, i.e., the system size and the centrality dependence of strange particle yields and ratios. In Sec. VI we focus on the equilibrium stages of the time evolution of central Au+Au collisions in connection to strangeness production in the (T, μ_B) plane and discuss the perspectives to identify a critical point in the phase diagram. We conclude this work with a summary in Sec. VII.

II. REMINDER OF THE PHSD TRANSPORT APPROACH

The parton-hadron-string dynamics (PHSD) is a microscopic covariant dynamical approach for strongly interacting systems in and out of equilibrium [21,22]. It is a transport approach which goes beyond the quasiparticle approximation, since it is based on Kadanoff-Baym equations for the Green's functions in phase-space representation in the first-order gradient expansion [25,26]. Including both a hadronic and a partonic phase as well as a transition between the effective degrees of freedom, PHSD is capable of describing the full time evolution of a relativistic heavy-ion collision. The theoretical description of the partonic degrees of freedom (quarks and gluons) is realized in line with the dynamical-quasiparticle model (DQPM) [26], which reproduces lQCD results in thermodynamical equilibrium and provides the properties of the partons, i.e., masses and widths in their spectral functions. In equilibrium the PHSD reproduces the partonic transport coefficients such as shear and bulk viscosities or the electric conductivity from lQCD calculations as well [27].

An actual nucleus-nucleus collision in PHSD follows the following steps:

(1) Primary hard scatterings between nucleons take place and produce excited color-singlet states, denoted by so-called strings (as described within the FRITIOF Lund model [28] and realized also in PYTHIA6.4 [29]). These strings decay into prehadrons with a formation time $\tau_f \sim 0.8$ fm/c and leading hadrons, which originate from the string ends and can reinteract with hadrons almost instantly with reduced cross sections (according to the constituent quark number).
(2) In the case in which the local energy density is above the critical value of $\epsilon_c \sim 0.5\,\mathrm{GeV/fm^3}$, the deconfinement is implemented by dissolving the newly produced hadrons into the massive colored quarks and antiquarks and mean-field energy from the DQPM.
(3) Within the QGP phase, the partons (quarks, antiquarks, and gluons) scatter and propagate in a self-generated mean-field potential. They are described as off-shell quasiparticles with temperature-dependent masses and widths, which are given by the DQPM.
(4) The expansion of the system is associated to a decrease of the local energy density and, once the local energy density becomes close to or lower than ϵ_c, the massive colored off-shell quarks and antiquarks hadronize to colorless off-shell mesons and baryons. The hadronization process is defined by covariant transition rates and fulfills the energy momentum and quantum number conservation in each event.
(5) In the hadronic corona as well as in the late hadronic phase, the particles are still interacting and propagating. Elastic and inelastic collisions among baryons, mesons, and resonances are implemented in PHSD and the

corresponding backward reactions are included through detailed balance for all channels.

We further note that the pure hadronic phase in PHSD is equivalent to the hadron-strings dynamics (HSD) model [30]. Accordingly, the comparison between PHSD and HSD calculations allows us to disentangle the role of the QGP phase in heavy-ion collisions. Even at low center-of-mass energies ($\sqrt{s_{NN}} \sim 3$ GeV) the PHSD and the HSD results slightly differ due to the appearance of QGP droplets in central cells of the system, which are characterized by high baryon and energy densities.

The PHSD approach has been tested for different colliding systems ($p+p, p+A, A+A$) in a wide range of bombarding energy, from AGS to LHC energies, and has been able to describe a large number of experimental observables, such as charged particle spectra, collective flow coefficients v_n, and electromagnetic probes such as photons and dileptons [27]. More recently, in Ref. [11], it has been also shown to provide a microscopic description of the maximum in the K^+/π^+ ratio in central nucleus-nucleus collisions. In the latter work we also found that the inclusion of CSR in the hadronic sector via string decay is crucial in order to reproduce the strangeness enhancement at AGS and lower SPS energies.

III. STRING FRAGMENTATION IN PHSD

A. Basic concepts

The string formation and decay represents the dominant particle-production mechanism in nucleus-nucleus collisions for bombarding energies from 2 to 160 A GeV. In PHSD, the primary hard scatterings between nucleons are described by string formation and decay in the FRITIOF Lund model [28]. A string is an excited color-singlet state, which is composed of two string ends corresponding to the leading constituent quarks of the colliding hadrons and a color flux tube in between. As the string ends recede, virtual $q\bar{q}$ or $qq\bar{q}\bar{q}$ pairs are produced in the uniform color field, breaking the string. Finally, the string decays into mesons or baryon-antibaryon pairs with formation time $\tau_f \sim 0.8$ fm/c (in the rest frame of the string).

In the string decay, the flavor of the produced quarks is determined via the Schwinger formula [29,31], which defines the production probability of massive $s\bar{s}$ pairs with respect to light flavor production ($u\bar{u}$,$d\bar{d}$) pairs:

$$\frac{P(s\bar{s})}{P(u\bar{u})} = \frac{P(s\bar{s})}{P(d\bar{d})} = \gamma_s = \exp\left(-\pi \frac{m_s^2 - m_{u,d}^2}{2\kappa}\right), \quad (1)$$

with $\kappa \approx 0.176\,\mathrm{GeV}^2$ representing the string tension and $m_{u,d,s}$ denoting the constituent quark masses for strange and light quarks. For the constituent quark masses $m_u \approx 0.35$ GeV and $m_s \approx 0.5$ GeV in the vacuum, the production of strange quarks is suppressed by a factor of $\gamma_s \approx 0.3$ with respect to the light quarks, which is the default setting in the FRITIOF routines. The relative production factors in PHSD/HSD have been readjusted in 1998 as follows [8]:

$$u:d:s:uu = \begin{cases} 1:1:0.3:0.07 & \text{at SPS to RHIC;} \\ 1:1:0.4:0.07 & \text{at AGS energies.} \end{cases} \quad (2)$$

The probability ratio γ_s has been increased to 0.4 at AGS energies in order to correctly reproduce the strangeness yield for $p+$Be collisions at AGS energies [8]. A smooth transition between the two values of γ_s is ensured by a linear interpolation as a function of the center-of-mass energy $\sqrt{s}$.

A further ingredient to fix the rapidity distribution for the newly produced hadrons is the fraction of energy and momentum that they acquire from the decaying string. This is defined by the fragmentation function $f(x,m_T)$, which is the probability distribution for a hadron with transverse mass m_T to be produced with an energy-momentum fraction x from the fragmenting string:

$$f(x,m_T) \approx \frac{1}{x}(1-x^a)\exp\left(-b\,m_T^2/x\right), \quad (3)$$

where $a = 0.23$ and $b = 0.34\,\mathrm{GeV}^{-2}$ as reliable settings for $p+p$ and $p+A$ collisions. As becomes evident from Eq. (3) the meson m_T scaling from string decay is included by default.

B. Modeling of the chiral symmetry restoration

In Ref. [11] the PHSD has been extended to include CSR in the string decay in a hadronic environment of finite baryon and meson density. Here we recall the main aspect of this extension which is based on the Hellman-Feynman theorem for the scalar quark condensate [32]. Accordingly, a linear decrease of the scalar quark condensate $\langle\bar{q}q\rangle$—which is nonvanishing in the vacuum due to a spontaneous breaking of chiral symmetry—is expected with baryon density ρ_B towards a chiral symmetric phase characterized by $\langle\bar{q}q\rangle \approx 0$ [33,34]. This decrease of the scalar quark condensate is expected also to lead to a change of the hadron properties with density and temperature, i.e., in a chirally restored phase the vector and axial vector currents should become equal [35–39]; the latter implies that, e.g., the ρ and a_1 spectral functions should become identical (as addressed above in the context of dilepton production). Since the scalar quark condensate $\langle\bar{q}q\rangle$ is not a direct observable, its manifestations should also be found indirectly in different hadronic abundances and spectra or particle ratios like K^+/π^+,$(\Lambda+\Sigma^0)/\pi^-$, etc., as advocated in Ref. [11].

In leading order the scalar quark condensate $\langle\bar{q}q\rangle$ can be evaluated in a dynamical calculation as follows [40]:

$$\frac{\langle\bar{q}q\rangle}{\langle\bar{q}q\rangle_V} = 1 - \frac{\Sigma_\pi}{f_\pi^2 m_\pi^2}\rho_S - \sum_h \frac{\sigma_h \rho_S^h}{f_\pi^2 m_\pi^2}, \quad (4)$$

where σ_h stands for the σ commutator of the relevant mesons h, $\langle\bar{q}q\rangle_V$ represents the vacuum condensate, $\Sigma_\pi \approx 45$ MeV is the pion-nucleon Σ term, and f_π and m_π are the pion decay constant and pion mass, respectively. Note, however, that the value of Σ_π is not so accurately known; a recent analysis points towards a larger value of $\Sigma_\pi \approx 59$ MeV [41,42] while actual lQCD results [43] suggest a substantially lower value. Accordingly, our following calculations—based on $\Sigma_\pi = 45$ MeV—have to be taken with some care, although in some sense it represents a world average (cf. Fig. 3 in Ref. [44]). According to the light quark content, the Σ term for hyperons is decreased by a factor of 2/3 for Λ and Σ hyperons and by a factor of 1/3 for Ξ baryons. Furthermore, for mesons

made out of light quarks and antiquarks, we use $\sigma_h = m_\pi/2$, whereas for mesons with a strange (antistrange) quark we consider $\sigma_h = m_\pi/4$. We mention here that improved results for the σ commutator for kaons can be obtained from chiral perturbation theory as in Ref. [45] and alternative assumptions for nonpseudoscalar mesons can be employed as suggested, e.g., by Cohen *et al.* in Ref. [32]. In view of the subleading contributions of these mesons to the ratio in Eq. (4) we keep the simple estimates noted above for our present study and look forward to a clarification of the present tension between the results from lQCD and dispersive approaches [46].

In Eq. (4), the quantities ρ_S and ρ_S^h denote the nucleon scalar density and the scalar density for a meson of type h, respectively. The scalar density of mesons h is evaluated in the independent-particle approximation as

$$\rho_S^h(x) = \frac{(2s+1)(2\tau+1)}{(2\pi)^3}\int d^3p \frac{m_h}{\sqrt{\mathbf{p}^2+m_h^2}} f_h(x,\mathbf{p}), \quad (5)$$

where $f_h(x,\mathbf{p})$ denotes the meson phase-space distribution [$x=(\mathbf{r},t)$] and s,τ refer to the discrete spin and isospin quantum numbers, respectively. Moreover, the vacuum scalar condensate $\langle\bar{q}q\rangle_V = \langle\bar{u}u\rangle_V + \langle\bar{d}d\rangle_V \approx 2\langle\bar{u}u\rangle_V$ can be computed according to the Gell-Mann-Oakes-Renner (GOR) relation [47,48],

$$f_\pi^2 m_\pi^2 = -\tfrac{1}{2}\left(m_u^0 + m_d^0\right)\langle\bar{q}q\rangle_V, \quad (6)$$

and gives $\langle\bar{q}q\rangle_V \approx -3.2\,\mathrm{fm}^{-3}$ for the bare quark masses $m_u^0 = m_d^0 \approx 7\,\mathrm{MeV}$. Finally, in Eq. (4) the nucleon scalar density ρ_S has to be determined in a suitable model with interacting degrees of freedom in order to match our knowledge on the nuclear EoS at low temperature and finite density. A proper (and widely used) approach is the nonlinear σ-ω model for nuclear matter, where ρ_S is defined as

$$\rho_S(x) = \frac{g_n}{(2\pi)^3}\int d^3p \frac{m_N^*}{\sqrt{\mathbf{p}_N^{*2}+m_N^{*2}}} f_N(x,\mathbf{p}), \quad (7)$$

where m_N^* and p_N^* denote the effective mass and momentum, respectively, and $f_N(x,\mathbf{p})$ is the phase-space occupation of a nucleon while the degeneracy factor is $g_n = 4$. In fact, in the nonlinear σ-ω model the nucleon mass is modified due to the scalar interaction with the medium:

$$m_N^*(x) = m_N^V - g_s\sigma(x), \quad (8)$$

where m_N^V denotes the nucleon mass in vacuum and $\sigma(x)$ is the scalar field which mediates the interaction between the nucleons and the medium with the coupling g_s. In order to calculate ρ_S, we need to determine the value of the scalar field $\sigma(x)$ at each space-time point x. This is done via the nonlinear gap equation [49,50]:

$$m_\sigma^2\sigma(x) + B\sigma^2(x) + C\sigma^3(x) = g_s\rho_S(x) = g_s g_n \int \frac{d^3p}{(2\pi)^3}\frac{m_N^*(x)}{\sqrt{\mathbf{p}^2+m_N^{*2}}} f_N(x,\mathbf{p}), \quad (9)$$

since for matter at rest we have $\mathbf{p}^* = \mathbf{p}$. In Eq. (9) the self-interaction of the σ field is included up to the fourth order. The parameters g_s, m_σ, B, C are fixed in order to reproduce the values of the nuclear matter quantities at saturation, i.e., the saturation density, the binding energy per nucleon, the compression modulus, and the effective nucleon mass. Actually, there are different sets for these quantities that lead to slightly different saturation properties. We defer a discussion on the uncertainties of our results to Sec. III C.

The main idea in Ref. [11] is to consider effective masses for the dressed quarks in the Schwinger formula (1) for the string decay in a hot and dense medium. The effective quark masses can be expressed in terms of a scalar coupling to the quark condensate $\langle\bar{q}q\rangle$ in first order as follows:

$$m_s^* = m_s^0 + \left(m_s^V - m_s^0\right)\frac{\langle\bar{q}q\rangle}{\langle\bar{q}q\rangle_V}, \quad (10)$$

$$m_q^* = m_q^0 + \left(m_q^V - m_q^0\right)\frac{\langle\bar{q}q\rangle}{\langle\bar{q}q\rangle_V}, \quad (11)$$

with $m_s^0 \approx 100\,\mathrm{MeV}$ and $m_q^0 \approx 7\,\mathrm{MeV}$ for the bare quark masses. In Eq. (10) the effective masses decrease from the vacuum values with decreasing scalar condensate $\langle\bar{q}q\rangle$ to the constituent masses. This adaptation of the Schwinger formula in case of a hot and dense medium implies a modification of the flavor production factors in Eq. (2). In an actual nucleus-nucleus collision, PHSD incorporates a dynamical calculation of all these features for each cell in space-time:

(1) the scalar density ρ_S is determined by solving the gap equation (9) for the σ field;
(2) the scalar condensate $\langle\bar{q}q\rangle$ is then computed via Eq. (4);
(3) the effective masses m_q^*, m_s^* are calculated according to Eqs. (10) and (11) and plugged in the Schwinger formula (1) in order to compute the flavor production ratios for the string decay.

We stress that, once the nucleon scalar density ρ_S and Σ_π are fixed, there is no additional parameter in the PHSD3.3 compared to the previous version PHSD3.2 that has been employed for a couple years for the analysis of relativistic heavy-ion reactions [27].

C. Dependence on the nuclear equation of state

In this section we analyze in more detail the flavor production ratios from the Schwinger formula in the presence of a hot and dense nuclear medium. As mentioned in the previous section there are different sets for the parameters g_s, m_σ, B, C in the gap equation (9). In fact, these parameters are fixed within the nonlinear σ-ω model in order to reproduce empirical values of nuclear matter quantities at saturation (i.e., saturation density, binding energy per nucleon, compression modulus, effective nucleon mass, etc.), but sizable uncertainties remain with respect to the high density properties. In Table I we display the values of g_s, m_s, B, C together with the vector coupling g_v, the vector meson mass m_v, the compression modulus K, and the ratio between the effective and the bare nucleon mass m^*/m at saturation density for three sets commonly indicated as NL1, NL2, and NL3. The sets NL1 and NL3 have the same compression modulus K but differ in the effective mass m^*/m at saturation density whereas NL1 and NL2 have the same effective mass but differ in the compression modulus K. By

TABLE I. Parameter sets NL1, NL2, and NL3 for the nonlinear σ-ω model employed in the transport calculations from Ref. [50].

	NL1	NL2	NL3
g_s	6.91	8.50	9.50
g_v	7.54	7.54	10.95
B (1/fm)	−40.6	50.57	1.589
C	384.4	−6.26	34.23
m_s (1/fm)	2.79	2.79	2.79
m_v (1/fm)	3.97	3.97	3.97
K (MeV)	380	210	380
m^*/m	0.83	0.83	0.70

comparing the results from NL1, NL2, and NL3 we will be able to explore separately the effects from the effective mass and compression modulus. In the context of the string decay, the most important parameter to focus on is the scalar coupling g_s, which is lower for the NL1 and NL2 set with respect to the corresponding values in the NL3 set. We show the dependence of the nucleon scalar density ρ_S on energy density ϵ in Fig. 1(a), the ratio between the scalar quark condensate and its value in the vacuum $\langle\bar{q}q\rangle/\langle\bar{q}q\rangle_V$ in Fig. 1(b), the light and strange quark effective masses m_q^*,m_s^* in Fig. 1(c), and the production probability of massive $s\bar{s}$ relative to light flavor production γ_s in Fig. 1(d). Note that an analogous dependence is observed with respect to the baryon density ρ_B since the energy density ϵ in leading order is just the nucleon mass times the baryon density. We find that all quantities plotted in Fig. 1 show practically identical results for NL1 (green dashed lines) and NL2 (thin orange lines) since the scalar density ρ_S essentially depends on the effective nucleon mass, which is very similar for NL1 and NL2 when plotted as a function of the energy density ϵ. The results shown in Fig. 1 are obtained at vanishing temperature $T = 0$, but all the following considerations can be extended to a more realistic picture at finite temperature (meson density) and illustrate the consequences of CSR in the PHSD results for heavy-ion collisions. The energy density ϵ here is calculated within the nonlinear σ-ω model by

$$\epsilon = U(\sigma) + \frac{g_v^2}{2m_v^2}\rho_N^2 + d\int \frac{d^3p}{(2\pi)^3}\, E^*(\mathbf{p})[N_f(\mathbf{p}) + N_{\bar{f}}(\mathbf{p})], \tag{12}$$

with

$$E^*(\mathbf{p}) = \sqrt{\mathbf{p}^2 + m_N^{*2}},$$
$$U(\sigma) = \frac{m_s^2}{2}\sigma^2 + \frac{B}{3}\sigma^3 + \frac{C}{4}\sigma^4,$$

where ρ_N represents the nucleon density and $N_f(\mathbf{p})$ and $N_{\bar{f}}(\mathbf{p})$ are the particle and antiparticle occupation numbers at fixed momentum $\mathbf{p}$, respectively.

The scalar density ρ_S increases with increasing energy density ϵ as displayed in Fig. 1(a). We find a moderate sensitivity to the nuclear equation of state up to energy densities of $\sim$0.5 GeV/fm^3 that are of relevance for the hadronic phase. In fact, the lines referring to the parameter sets NL1/NL2 and NL3 show very similar behavior as a function

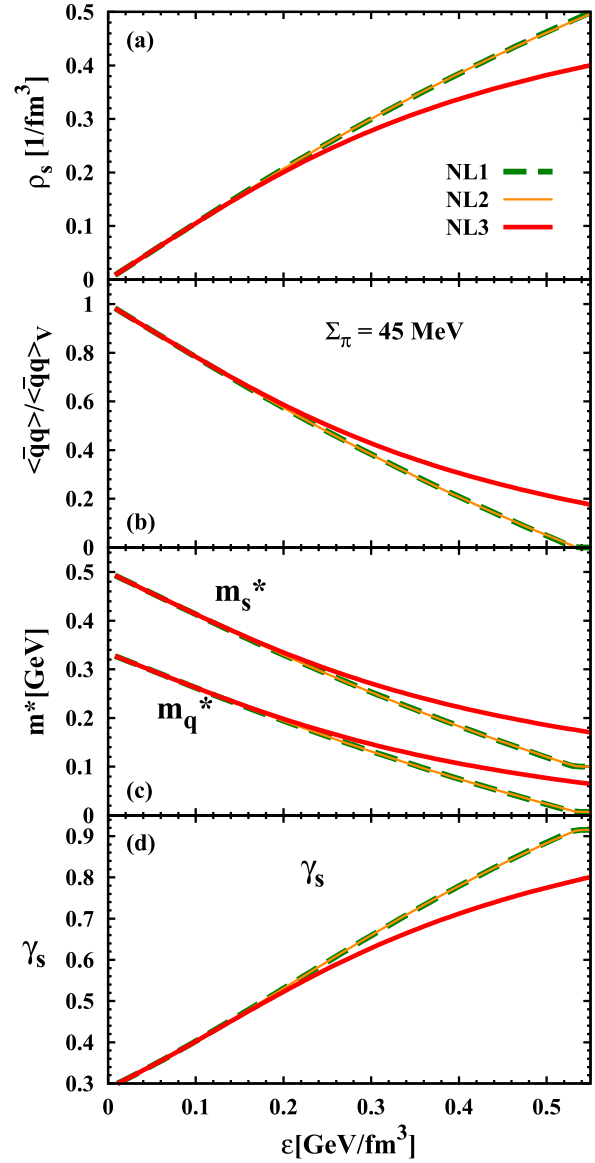

FIG. 1. The nucleon scalar density ρ_S (a), the ratio between the scalar quark condensate and its value in the vacuum $\langle\bar{q}q\rangle/\langle\bar{q}q\rangle_V$ (b), the light and strange quark effective masses m_q^*,m_s^* (c), and the production probability of massive $s\bar{s}$ relative to light flavor production γ_s (d) as a function of the energy density ϵ for the parameter sets NL3 (red solid lines), NL2 (thin orange lines), and NL1 (dashed green lines) at $T = 0$ and with $\Sigma_\pi = 45$ MeV.

of ϵ, but the NL3 (solid line) set is always characterized by lower values of the scalar density ρ_S relative to the NL1 or NL2 parametrization (dashed line). This is due to the larger value of the effective nucleon mass m_N^* in case of the NL1 and NL2 parameter sets. In Fig. 1(b), the ratio $\langle\bar{q}q\rangle/\langle\bar{q}q\rangle_V$ is presented as a function of ϵ. At $\epsilon = 0$ the scalar condensate corresponds to the vacuum value $\langle\bar{q}q\rangle_V$ and for fixed $\Sigma_\pi = 45$ MeV it decreases almost linearly with increasing energy density and almost vanishes for the critical energy density $\epsilon_c \approx 0.5$ GeV/fm^3. In this case, the order between NL1/NL2 and NL3 results is reversed: The NL3 parametrization for the nuclear EoS is associated to higher

values of the scalar quark condensate with respect to the NL1 or NL2 sets. This feature can be easily explained looking at the definition of the ratio $\langle\bar{q}q\rangle/\langle\bar{q}q\rangle_V$ (4): At $T = 0$, there are no thermal mesons, and thus the last term of the relation vanishes and the ratio is entirely fixed by the scalar density ρ_S; hence, higher values of ρ_S correspond to lower values of $\langle\bar{q}q\rangle/\langle\bar{q}q\rangle_V$. Therefore, the NL1 and NL2 parametrizations are characterized by lower values of the scalar quark condensate with respect to the NL3 parameter set. It follows that the light and strange quark effective masses m_q^*,m_s^* in of Fig. 1(c) show a very similar dependence on the energy density. At vanishing energy density ϵ, the quark effective masses are equal to their vacuum values, $m_q \approx 0.33$ GeV and $m_s \approx 0.5$ GeV; with increasing ϵ the quark masses decrease in line with the scalar quark condensate up to their bare values $m_s^0 \approx 100$ MeV and $m_q^0 \approx 7$ MeV for vanishing $\langle\bar{q}q\rangle/\langle\bar{q}q\rangle_V$. The decrease of both m_q and m_s is approximately linear in energy density where the slope associated to the light quark is flatter in comparison to the strange quark mass. Concerning the comparison between the different choices for the nuclear equation of state, we find also for these masses a non-negligible sensitivity and the same hierarchy as for the scalar quark condensate (the results associated to NL1/NL2 are always below the corresponding results for NL3).

We recall that the effective masses of the quarks enter the Schwinger formula (1) for the hadronic particle production via the string decays. In Fig. 1(d) the strangeness ratio γ_s is shown as a function of energy density for the two parameter sets. The factor γ_s increases from the vacuum case ($\gamma_s \approx 0.3$) with increasing energy density up to values of 0.8–0.9 for $\epsilon \approx \epsilon_c$. Thus the production of a $s\bar{s}$ pair relative to a light quark pair is no longer suppressed close to the phase boundary for CSR as it is in vacuum. The reason for this increase is the steeper decrease of the effective strange quark mass (with energy density) in comparison to the effective light quark mass as mentioned above. Furthermore, the NL1 and NL2 parametrizations give larger values of γ_s than the NL3 parametrization due to a faster change of the masses with ϵ [cf. Fig. 1(c)].

We note in extension of Ref. [11] that this scheme for CSR in the string decay mechanism can be applied not only to the light and strange quarks, but also to diquark combinations that are additionally produced in the fragmentation of the string and lead finally to baryon-antibaryon pairs. Here the default JETSET ratios fix the diquark mass in the vacuum; e.g., a light diquark mass in vacuum of $m_{uu}^V = 0.65$ GeV leads to a suppression of a light diquark pair relative to a light quark-antiquark pair of

$$\frac{P(uu\bar{u}\bar{u})}{P(u\bar{u})} \approx 0.07\,. \tag{13}$$

For the creation of a diquark (su) one employs $m_{su}^V \approx 0.725$ GeV, which leads to the ratio for a (su)-diquark pair relative to a light (uu)-diquark pair of

$$\frac{P(su\bar{s}\bar{u})}{P(uu\bar{u}\bar{u})} \approx 0.4\,. \tag{14}$$

Within the same line the vacuum mass of a ss diquark can be determined from JETSET. The Schwinger mechanism of string decay in vacuum thus requires the following dressed vacuum masses: $m_u^V \approx 0.35$ GeV, $m_s^V \approx 0.5$ GeV, $m_{uu}^V \approx 0.65$ GeV, $m_{su}^V \approx 0.725$ GeV, and $m_{ss}^V \approx 0.87$ GeV to comply with experimental observation in nucleon-nucleon collisions. The production probability of diquarks (su) relative to uu diquarks (14) and (ss) relative to uu diquarks does not change very much in the dense medium—in line with (indirect) experimental observation—and since $m_{su}^0 - m_{uu}^0 \approx m_s^0 - m_u^0$, the bare diquark masses m_{uu}^0 can be fixed and give $m_{uu}^0 \approx 0.5$ GeV, $m_{su}^0 \approx 0.593$ GeV, and $m_{ss}^0 \approx 0.763$ GeV. The explicit variations of the flavor ratios with the energy density are displayed in Fig. 2 and show that the diquark ratios only very moderately change with the energy density whereas the s/u ratio steeply rises with ϵ. We specify once more that these results have been obtained within a pure hadronic system at vanishing temperature, but the conclusions are valid also for finite temperatures (meson densities).

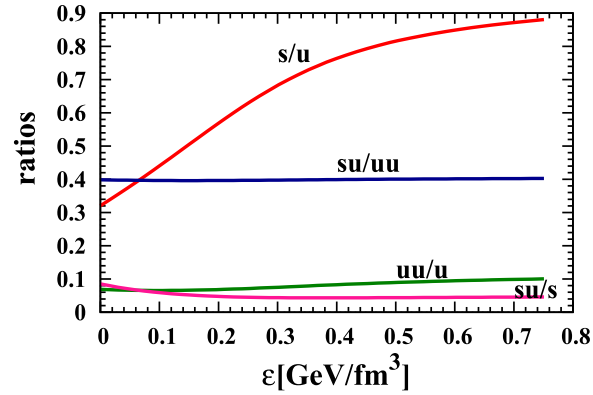

FIG. 2. The quark and diquark ratios in the string decay (hadronic environment) as a function of the energy density ϵ as evaluated within the nonlinear σ-ω model for the parameter set NL3 for $T = 0$.

The variations of the ratios in Fig. 2, however, are limited to the hadronic phase with energy densities below ϵ_c. Above $\epsilon_c \approx 0.5\,\mathrm{GeV/fm^3}$ strings cannot be formed anymore due to a vanishing string tension κ in the QGP and the hadrons dissolve to partonic degrees of freedom (and mean-field energy). Consequently, the s/u factor finally shows an increase for $\epsilon < \epsilon_c$ (associated to CSR) and in correspondence of $\epsilon \geqslant \epsilon_c$ it drops to the value $\sim 1/3$ (fixed by comparison with the strangeness production at RHIC and LHC energies observed experimentally). The energy dependence of the s/u ratio including the QGP phase has been shown already in Fig. 2 of Ref. [11]. We recall that in the partonic phase the s/u ratio remains constant as a function of the energy density. As a result we can identify a so-called horn structure in the s/u ratio as a function of ϵ, where the initial increase is related to chiral symmetry restoration in the hadronic phase and the subsequent sharp decrease is associated to the formation of the QGP. We thus expect that CSR modifies the particle abundances and spectra (especially in the strange particle sector) from heavy-ion collisions, where increasing energy densities ϵ in the overlap region can be achieved with increasing bombardment energy (at the same centrality of the collision).

D. Impact of $3M \leftrightarrow B\bar{B}$ collisions on the strangeness production

For a solid study of the differential spectra of strange and nonstrange particles it is essential that both are treated on the same level in many-body theory. Whereas in earlier PHSD studies the three-body channels incorporating three mesons in the production of baryon-antibaryon pairs in line with Ref. [51] (e.g., $\rho + \rho + \pi \leftrightarrow N + \bar{N}$) have been incorporated by default in the nonstrange sector, the corresponding channels in the strangeness sector (e.g., $\rho + K^* + \pi \leftrightarrow \bar{N} + Y$, etc.) had been discarded in PHSD3.2. Nevertheless, the possible impact of such channels on the observables of interest in this study has to be examined in order to control the consistency of the approach. Accordingly, in this subsection we present the influence of an extended description of $3M \leftrightarrow B\bar{B}$ reactions to the strange sector on the rapidity spectra from central heavy-ion collisions with and without CSR.

To this aim we have generalized the quark rearrangement model, first presented in Ref. [51] for the light (u,d) sector to the strange sector. The details of the extended model will be given in an upcoming study where also the explicit tests of detailed balance relations on a channel-by-channel basis are demonstrated as well as the particular impact on multistrange antibaryon production and annihilation. By including the strangeness sector the number of individual three-body (mass channels) amounts to more than 2500, including also the fusion of three kaons (or K^*'s) to the $N + \bar{\Omega}$ channel. We also consider the hidden strangeness of the η and the Φ mesons with proper weights for channels where either the light quarks or $s\bar{s}$ are rearranged. As in Ref. [51] the matrix elements for the transitions are provided by experimental data on baryon-antibaryon annihilation.

Without going into further details we show in Fig. 3—exemplary for other particles—the rapidity spectra of $\Lambda + \Sigma^0$ baryons at 8, 30, and 158 A GeV in central Au + Au collisions with (solid lines) and without (dashed lines) chiral symmetry restoration as well as with (blue lines) and without (red lines) the extended strangeness $3M \leftrightarrow B\bar{B}$ reactions. In general, the inclusion of chiral symmetry restoration enhances the number of produced $\Lambda + \Sigma^0$ baryons at all energies. This is most pronounced for the lower energies of 8 and 30 A GeV (cf. the detailed studies in the next section). In particular for the lower energies there is no visible difference in the rapidity spectra for the extended $3M \leftrightarrow B\bar{B}$ reactions. Only at 158 A GeV does one find a slight difference ($\sim$1%) in the central rapidity region. The reason for these findings is related to the low abundance of mesons carrying a strange quark at low bombarding energies and additionally in the heavier masses of the hyperons, which induces a lower phase space for production, since the transition probability is directly proportional to the available phase space in the flavor rearrangement model of Ref. [51]. We conclude that the extended three-body reactions with strangeness have no crucial impact at AGS and SPS energies.

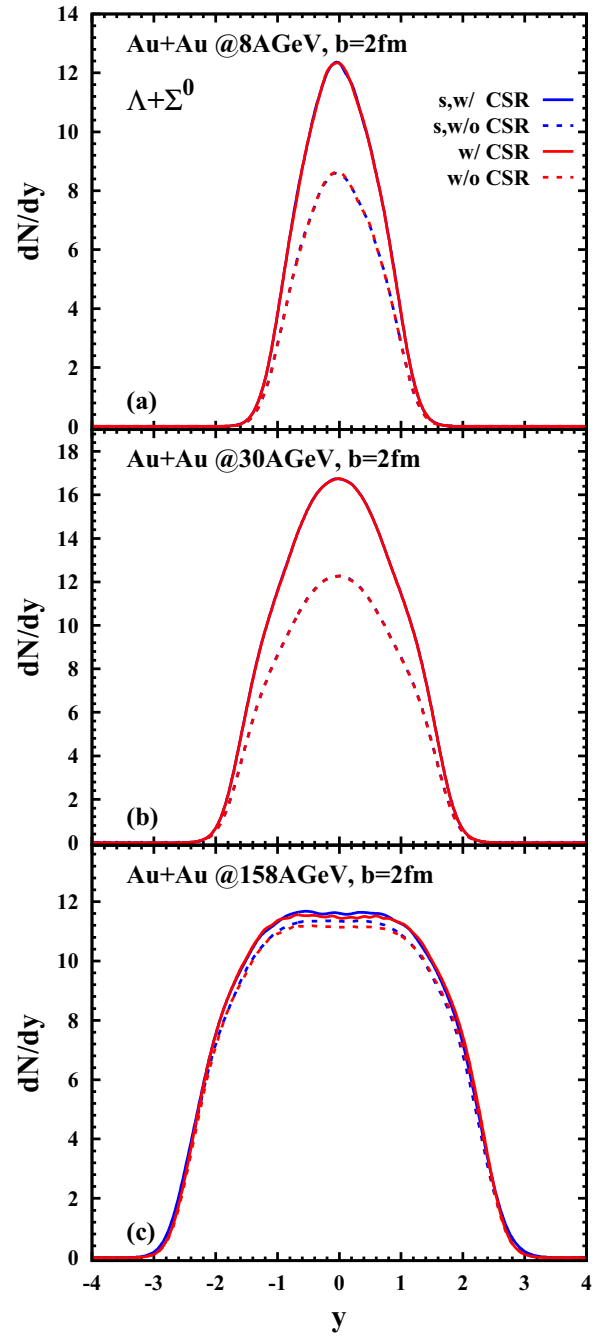

FIG. 3. Rapidity spectra for $\Lambda + \Sigma^0$ baryons in 5% central Au+Au collisions for the energies of 8 (a), 30 (b), and 158 A GeV (c) with (solid lines) and without CSR (dashed lines). The blue lines stand for the results that include the new three-meson reactions with strangeness content while the red lines display results when incorporating only nonstrange three-meson channels.

IV. APPLICATION TO NUCLEUS-NUCLEUS COLLISIONS

In this section we study observables from heavy-ion collisions with respect to different aspects that had not been considered in Ref. [11]. In this respect we present results for the rapidity distribution of the most abundant particles at AGS and SPS energies for different nuclear equations of state in order to estimate the uncertainties of our approach. In addition we also explore the impact of CSR on the transverse dynamics by calculating the transverse mass spectra for protons, pions, kaons, and antikaons in comparison to available data. We recall that in particular the transverse slopes of the kaon spectra

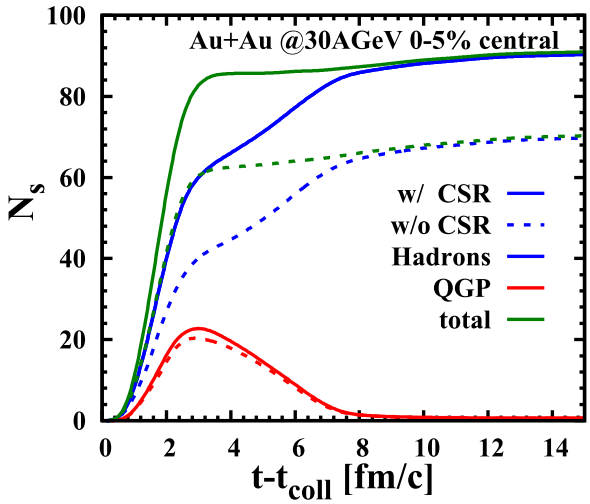

FIG. 4. The strange particle number N_s as a function of time in 5% central Au+Au collision at 30 A GeV. The solid lines show the results from PHSD including CSR with NL1 parameters, while the dashed lines show the results from PHSD without CSR. The green lines refer to the total number of strange particles, while the blue and red lines refer to the hadronic and partonic contributions of the strangeness content, respectively.

had been clearly underestimated in the earlier HSD studies (without a partonic phase) [9]. As a survey we present the excitation functions of particle yields and ratios together with the uncertainty due to the nuclear EoS. Moreover, we show the time evolution of the number of strange particles and the corresponding production rates from the different production channels. The following scenarios will be explored:

(1) default PHSD calculations without CSR;
(2) PHSD calculations including CSR with NL3 as parameter set for the nuclear EoS;
(3) PHSD calculations including CSR with NL2 as parameter set for the nuclear EoS;
(4) PHSD calculations including CSR with NL1 as parameter set for the nuclear EoS.

A. Time evolution of the strange particle multiplicities

At AGS and SPS energies the strange particle production takes place at the early stages of the collision process, as seen from Fig. 4, where the number of particles containing s quarks N_s is plotted (green solid and dashed lines) as a function of time in central Au+Au collision at a bombardment energy of 30 A GeV for the 5% most central collisions. More than ≈90% of the strange content of the system is created in the time interval between 0 and 4 fm/c after the collision and already at about 8 fm/c strange particles are not produced anymore. In Fig. 4 the total number of strange particles has also been separated in the corresponding hadronic and partonic contributions, represented by the blue and red lines, respectively. At the energy of 30 A GeV, the hadronic strangeness content is dominant relative to the partonic one, which can reach ∼25% of the total strangeness content in correspondence with the maximum value of the partonic contribution. The strange quarks in the partonic phase appear in the system not immediately after the collision but after about 1.5 fm/c. In fact, the primary interactions within the PHSD are realized via string excitation, and after that in the cells with energy density $\epsilon > 0.5\,\mathrm{GeV/fm^3}$ the hadrons are dissolved into partons and mean field energy. The partonic N_s distribution initially increases as a function of time, reaching a maximum at about 3 fm/c. Then at larger times the energy density of the system decreases; as a result the partons hadronize by dynamical coalescence which lasts up to about 8 fm/c, when the strange hadron number is basically fixed. We can conclude that at 30 A GeV the steep increase of the number of strange particles as a function of time has to be attributed dominantly to the hadronic production, which occurs in PHSD via string formation and decay. The other hadronic scattering processes, which are not negligible at this bombarding energy, do not create further strangeness in the system, but they are only responsible for strange flavor exchanges.

It is, furthermore, interesting to compare the strange particle amount computed in PHSD including and excluding CSR in the string dynamics. In Fig. 4 we show PHSD calculations only in the limits: without CSR (dashed lines) and including CSR with NL1 as parameter set (solid lines). The restoration of chiral symmetry causes a sizable increase (≈30%) of the total strangeness content. We notice that CSR does not modify the time evolution of $N_s(t)$, but it only affects the hadronic contribution to the strange particle production. There is a slight difference between the partonic results with and without CSR since the strange particle number in the partonic phase is slightly higher when including CSR. This is, however, not due to a higher strangeness production in the QGP, but stems from particles, which are produced by string decay in the hadronic corona and travel to cells with energy density above ϵ_c during their propagation. Thus such strange particles, even if produced by the string decay, dissolve into partonic degrees of freedom. In this respect the enhancement of the strange particle number in the hadronic phase drives a small increase also in the partonic contribution of N_s.

To provide a more complete illustration of the time evolution of the strangeness content in a heavy-ion collision we show in Fig. 5 the rate dN_s/dt of strange particles at 8 [Fig. 5(a)], 30 [Fig. 5(b)], and 158 A GeV [Fig. 5(c)] in central collisions. We show again the total strange particle rate in green, the hadronic contribution in blue, and the partonic contribution in red, comparing in all cases the calculations with and without CSR by the solid and dashed lines, respectively. We mention that these rates include production as well as losses either due to dissolution of hadrons in the QGP or due to hadronization of strange partons. Accordingly these rates become negative when dissolution or hadronization dominates. As already seen in Fig. 4, the strange particle production occurs at the first stages of the collisions and the strangeness production rate increases with increasing bombarding energy. The hadronic contribution is dominant at the collision energies $E_{\mathrm{Lab}} = 8$ and 30 A GeV, while the partonic production rate is larger than the hadronic one at $E_{\mathrm{Lab}} = 158$ A GeV. The strangeness enhancement associated to CSR is most clearly visible at lower energies while at 158 A GeV it is very moderate. We will find the same result on the final particle rapidity spectra

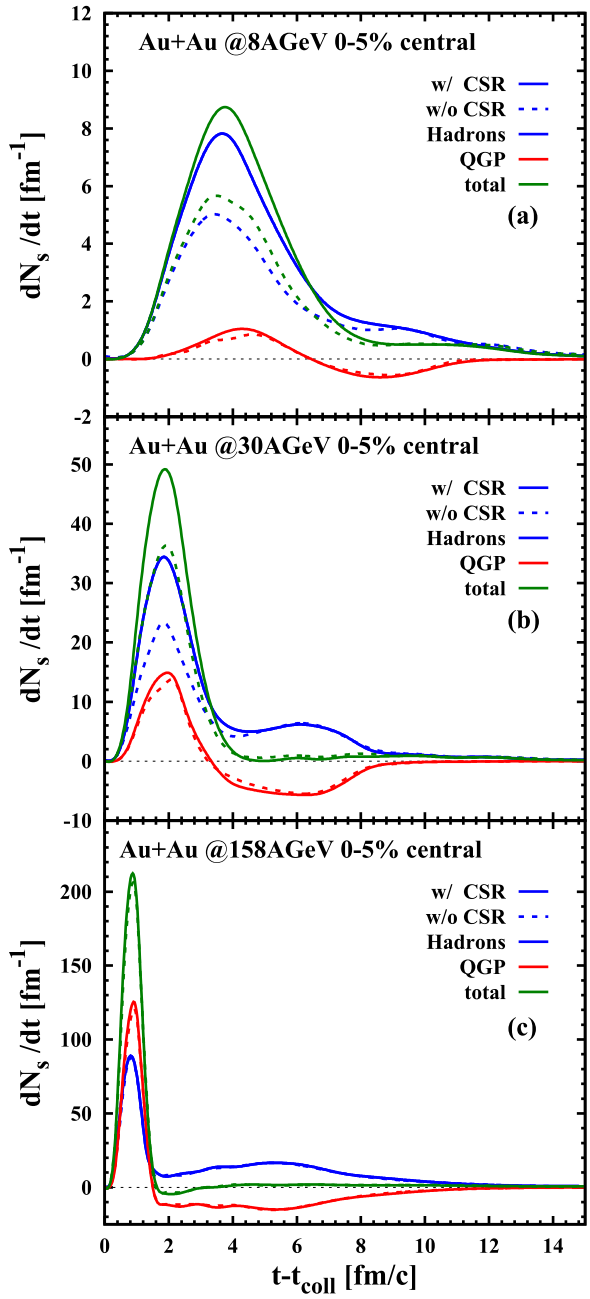

FIG. 5. The strangeness rate dN_s/dt as a function of the time in 5% central Au+Au collisions at 8 (a), 30 (b), and 158 A GeV (c). The coding of the lines is the same as in Fig. 4. Note that these rates become negative when strange hadron dissolution or strange parton hadronization dominate, respectively.

(see next subsection). The total strange particle rate remains positive during the entire time evolution in Figs. 5(a) and 5(b) and shows a small negative rate only for $E_{\rm Lab} = 158$ A GeV due to the dissolution of strange hadrons in the QGP; on the other hand the partonic rate becomes negative at larger times since the hadronization (loss) dominates the strange quark production. The negative rate on the partonic side is balanced by the positive rate on the hadronic side due to strangeness conservation.

Comparing the rates at the different energies, we can see that the strangeness production is slower at lower energies. In fact, the peak of the total dN_s/dt shifts to smaller times with increasing energies, and for $E_{\rm Lab} = 158$ A GeV the whole strangeness production occurs within 2 fm/c. On the other hand the duration of the hadronization process becomes longer at higher bombarding energies, where a larger volume of the systems turns into the QGP phase. In general, after $\approx$12 fm/c the strangeness content is fixed and within PHSD the creation of strange particles ceases. Equilibrium aspects of the strangeness production will be discussed in Sec. VI.

B. Rapidity spectra at AGS and SPS energies

We present in Figs. 6 to 8 the PHSD results for the rapidity distribution of protons, $(\Lambda + \Sigma^0)$'s, pions, and kaons for central nucleus-nucleus collisions at different energies (from AGS to top SPS energies) in comparison to the experimental data from Refs. [52–58]. The following scenarios will be explored at different energies:

(1) default PHSD calculations without CSR, represented by the dotted blue lines;
(2) PHSD calculations including CSR with NL3 as parameter set for the nuclear EoS, represented by the solid red lines;
(3) PHSD calculations including CSR with NL1 as parameter set for the nuclear EoS, represented by the dashed green lines.

We note that PHSD calculations for the parameter set NL2 are not shown explicitly since the results are in between those for NL1 and NL3. We will come back to an explicit comparison below. The results of the first two scenarios are almost equivalent to the PHSD calculations shown in the previous study [11], with a slight difference regarding the proton and meson spectra. This is due to a few recent upgrades in PHSD: The first concerns the extension of inelastic meson-meson scattering above 1.3 GeV of invariant energy $\sqrt{s}$ to string formation and decay with a cross section of $\sim$10 mb; the second improvement is related to p-wave scattering in the reaction channel $\pi + N \leftrightarrow \Delta$, which had been treated isotropically before. Note, however, that the study in Ref. [11] had a focus on the comparison of HSD and PHSD calculations in order to examine also the role of partonic degrees of freedom, whereas here we concentrate on the variation of the spectra with respect to the nuclear EoS employing only the updated PHSD3.3 calculations.

First, we compare the results with and without CSR at $E_{\rm Lab} = 10.7$ A GeV (Fig. 6), to point out the general effect of this mechanism on the final particle rapidity distributions and in particular show the dependence on the parameter sets NL1 and NL3 for the nonlinear σ-ω model for the nuclear EoS in extension to Ref. [11]. The restoration of chiral symmetry gives an enhancement of the strange particle yields both for mesons and baryons. On the other hand, it produces a slight decrease in the number of pions at midrapidity due to the suppression of pions in the string decays in favor of strange hadrons. The proton rapidity spectra do not present any sensible variation; in fact the CSR as implemented in PHSD modifies essentially

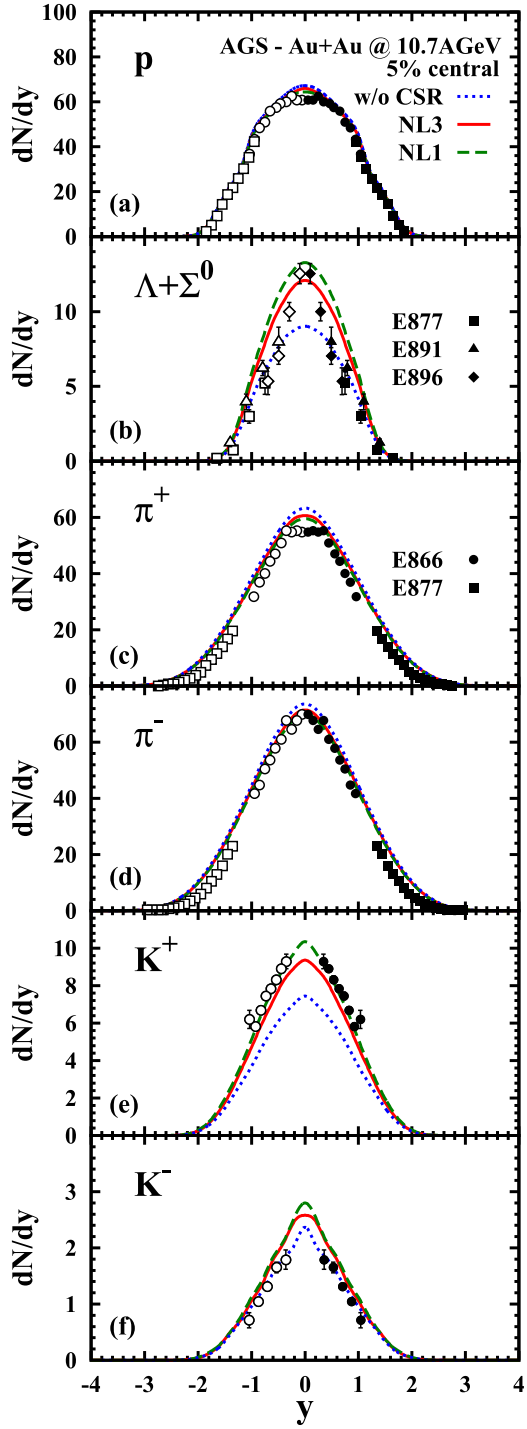

FIG. 6. The rapidity distribution of protons, $(\Lambda + \Sigma^0)$'s, pions, and kaons for 5% central Au+Au collisions at 10.7 A GeV in comparison to the experimental data from Refs. [52,53]. The solid (red) lines show the results from PHSD including CSR with NL3 parameters, the dashed green lines show the results from PHSD including CSR with NL1 parameters, and the blue dotted lines show the result from PHSD without CSR.

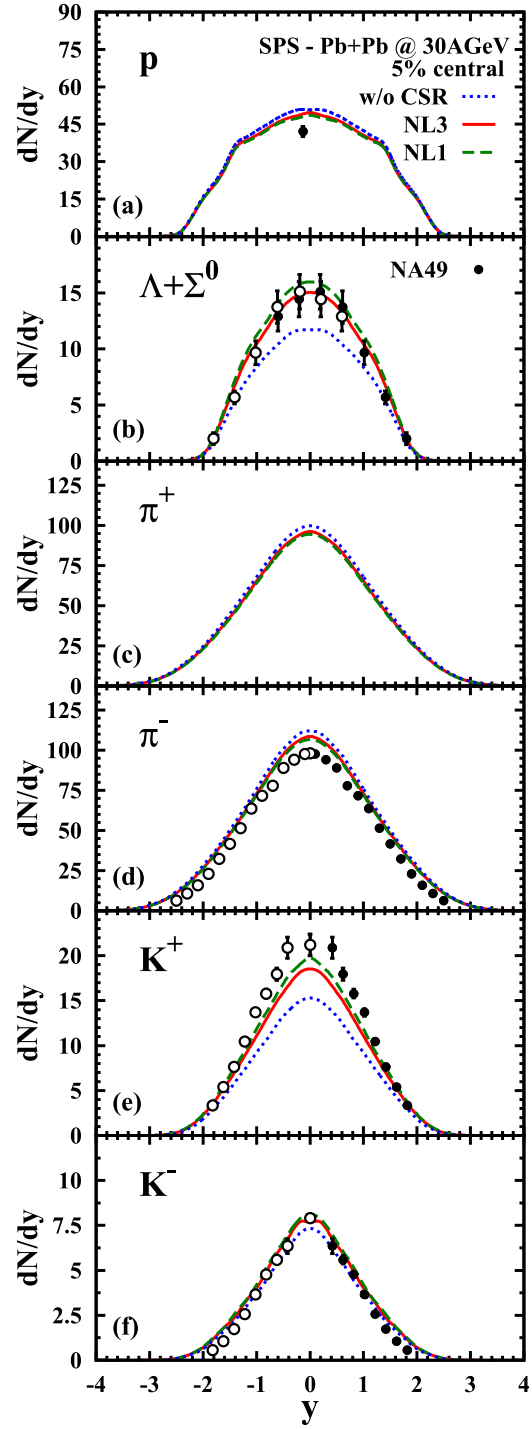

FIG. 7. The rapidity distribution of protons, $(\Lambda + \Sigma^0)$'s, pions, and kaons for 5% central Au+Au collisions at 30 A GeV in comparison to the experimental data from Ref. [54–56]. The coding of the lines is the same as in Fig. 6.

the chemistry of the newly produced particles in the string decay and has a minor impact the dynamics of the nucleons, which in the string picture are associated to the string ends of the primary interactions in the system. The inclusion of the CSR is essential in order to correctly reproduce the strange particle rapidity spectra, as we can see especially for $(\Lambda + \Sigma^0)$ hyperons and K^+ mesons. Furthermore, our calculations for the proton rapidity spectra are in good agreement with experimental observation.

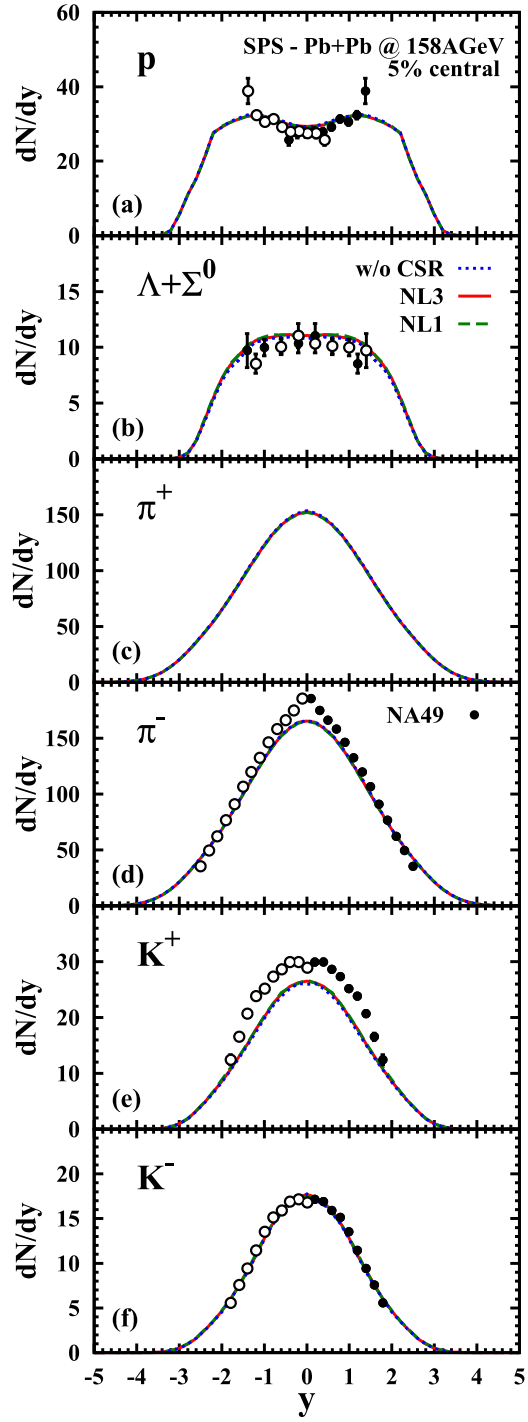

FIG. 8. The rapidity distribution of protons, $(\Lambda + \Sigma^0)$'s, pions, and kaons for 5% central Au+Au collisions at 158 A GeV in comparison to the experimental data from Ref. [57,58]. The coding of the lines is the same as in Fig. 6.

Next, we discuss the results from PHSD with CSR using two different parametrizations for the nuclear equation of state, i.e., NL3 and NL1. The general features of the strangeness enhancement hold for both parametrizations; in particular the NL1 set provides larger values for all strange particle rapidity spectra at midrapidity in line with the discussion of Fig. 1.

TABLE II. Particle abundances and strange to nonstrange particle ratios at midrapidity ($|y| \leqslant 0.5$) from 5% central Pb+Pb collisions at 30 A GeV.

	NL1	NL2	NL3
p	47.6	48.2	48.5
π^+	91.1	91.7	92.5
π^-	102.7	103.3	104.2
K^+	18.6	18.1	17.6
K^-	7.58	7.45	7.34
$\Lambda + \Sigma^0$	15.6	15.1	14.7
K^+/π^+	0.204	0.197	0.190
K^-/π^-	0.0738	0.0721	0.0704
$(\Lambda + \Sigma^0)/\pi$	0.0537	0.0516	0.0498

The difference between the two parametrizations represents the uncertainty of our results related to CSR as implemented in PHSD. We stress that we do not tune the parameters of the equation of state to fit the data, but we employ different nuclear EoS to compute the scalar density (as explained in Sec. III C) in order to explore the uncertainties of our approach.

In Fig. 7 the rapidity spectra of various hadrons at $E_{\rm Lab} = 30$ A GeV are shown. We find the same features as for $E_{\rm Lab} = 10.7$ A GeV concerning the strangeness enhancement and the comparison between the two parameter sets for the equation of state; the differences are slightly smaller at this energy. At midrapidity, both protons and pions are very slightly overestimated in all explored scenarios, which suggests that the nuclear stopping is still a bit overestimated. Finally, at the top SPS energy $E_{\rm Lab} = 158$ A GeV (Fig. 8) the CSR does not play a significant role, since the dynamics is dominated by the QGP phase. Thus, there is no appreciable difference between the results with and without CSR for the two different EoS. Our results for π^- and K^+ are lower with respect to the experimental data; however, the $(\Lambda + \Sigma^0)$ and K^- as well as the protons are correctly reproduced. It is presently unclear where these final differences stem from, since strangeness conservation is exactly fulfilled in the PHSD calculations.

As we have seen in Fig. 1 the results for the strangeness ratio $\gamma_s(\epsilon)$ are very similar for the parameter sets NL1 and NL2 for nuclear matter at $T = 0$. In heavy-ion collisions, however, the different compression modulus leads to a slightly different baryon dynamics, which also has an impact on the meson abundances and spectra. In order to quantify the effect of the different nuclear EoS on the particle abundances we provide in Table II the midrapidity densities for protons, pions, K^+, K^-, and $\Lambda + \Sigma^0$ as well as their ratios for the parameter sets NL1, NL2, and NL3 in case of a central Pb+Pb collision at 30 A GeV, where the effect from CSR is most pronounced. As one can extract from the table, the proton and pion densities at midrapidity are correlated: a higher stopping goes along with a higher pion density with the order NL3 > NL2 > NL1. On the other hand the strangeness densities at midrapidity are anticorrelated with the proton density; we obtain the order NL1 > NL2 > NL3. Although the hadron densities differ, not so dramatically, it gives an enhanced effect in ratios

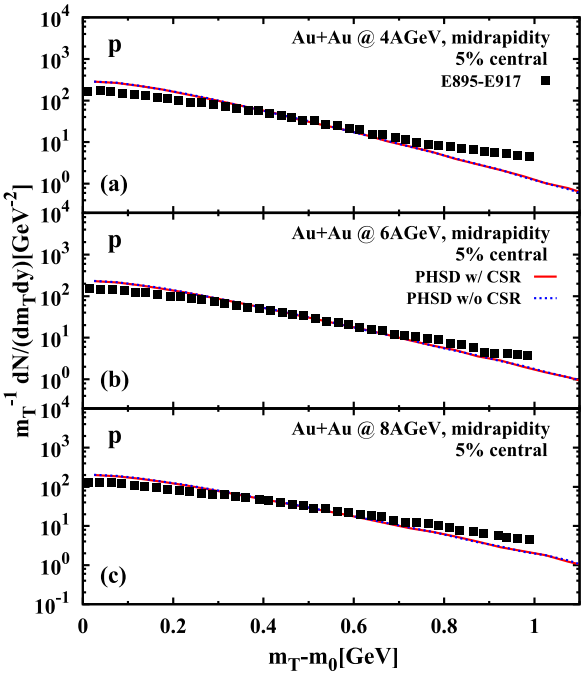

FIG. 9. The transverse mass spectra of protons for 5% central Au+Au collisions at 4, 6, and 8 A GeV in comparison to the experimental data from Ref. [59]. The solid (red) lines show the results from PHSD including CSR with NL3 parameters; the dotted (blue) lines show the results from PHSD without CSR.

K^+/π^+, K^-/π^-, and $(\Lambda + \Sigma^0)/\pi$ in the order NL1 > NL2 > NL3. Since any realistic nuclear EoS is expected to provide results within the limits of these parameter sets we expect to obtain reliable bounds on the uncertainties with respect to the nuclear EoS.

C. Transverse mass spectra at AGS and SPS energies

We recall that in earlier HSD calculations (without a partonic phase) the slopes of the transverse mass distributions have been severely underestimated [9]. In an extension of Ref. [11] we show in this section the PHSD results for the transverse mass spectra of protons, pions, and kaons for different energies in central Au+Au collisions in Figs. 9 and 10 and Pb+Pb collisions in Figs. 11 and 12 in comparison with AGS and SPS data, respectively. We do not show the further scenarios (PHSD calculations including CSR with NL1 or NL2) since the differences with respect to the parameter set NL3 for CSR are practically not visible.

At AGS energies (Fig. 9), i.e., $E_{\rm Lab} = 4$, 6, and 8 A GeV, our calculations for the proton spectra show the same trend as the experimental data. However, we observe that the computed spectra are softer than the experimental data in this energy regime. In fact, our results overestimate the data at low transverse mass m_T and underestimate the data at larger m_T. Note, however, that in our present calculations hadronic potentials have not been included. We leave the study of explicit hadronic potentials in the propagation of the degrees of freedom to a future work. We notice that CSR produces no change in the transverse mass spectra of the protons, both

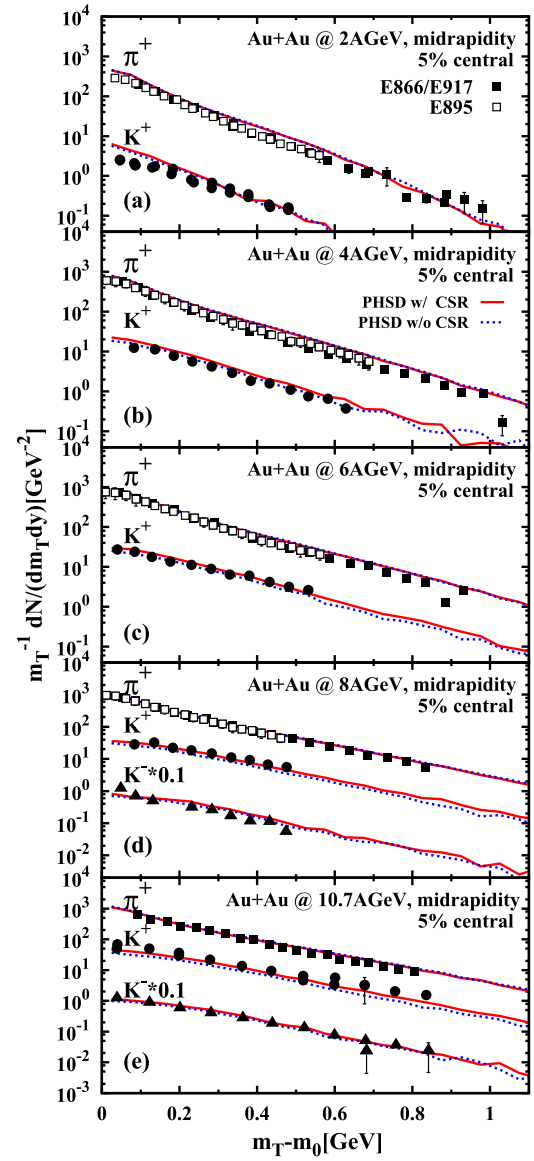

FIG. 10. The transverse mass spectra of pions and kaons for 5% central Au+Au collisions at 2, 4, 6, 8, and 10.7 A GeV in comparison to the experimental data from Refs. [60,61]. We show the results from PHSD including CSR with NL3 parameters by solid (red) lines and those from PHSD without CSR by dotted (blue) lines.

at AGS energies (Fig. 9) and at SPS energies (Fig. 11). At larger energies, i.e., $E_{\rm Lab} = 20$, 30, 158 A GeV (Fig. 11), the PHSD results are in a good agreement with the experimental data for protons. In the latter cases, a sizable volume of the system performs a phase transition to the QGP and the final particle spectra are not sensitive to hadronic potentials anymore because the baryon densities in the final hadronic phase are rather low.

In Figs. 10 and 12 we display the transverse mass spectra for pions and kaons in central Au+Au collisions at AGS energies and in Pb+Pb collisions at SPS energies, respectively. We focus on the role played by the CSR on the mesons transverse mass spectra. At the lower energies, $E_{\rm Lab} = 2$ A GeV, there

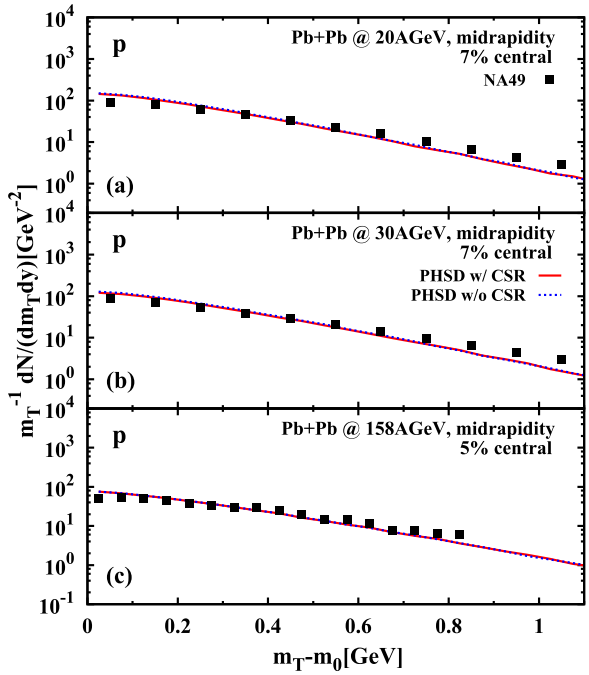

FIG. 11. The transverse mass spectra of protons for 5% and 7% central Pb+Pb collisions at 20, 30, and 158 A GeV in comparison to the experimental data from Ref. [62]. The coding of the lines is the same as in Fig. 9.

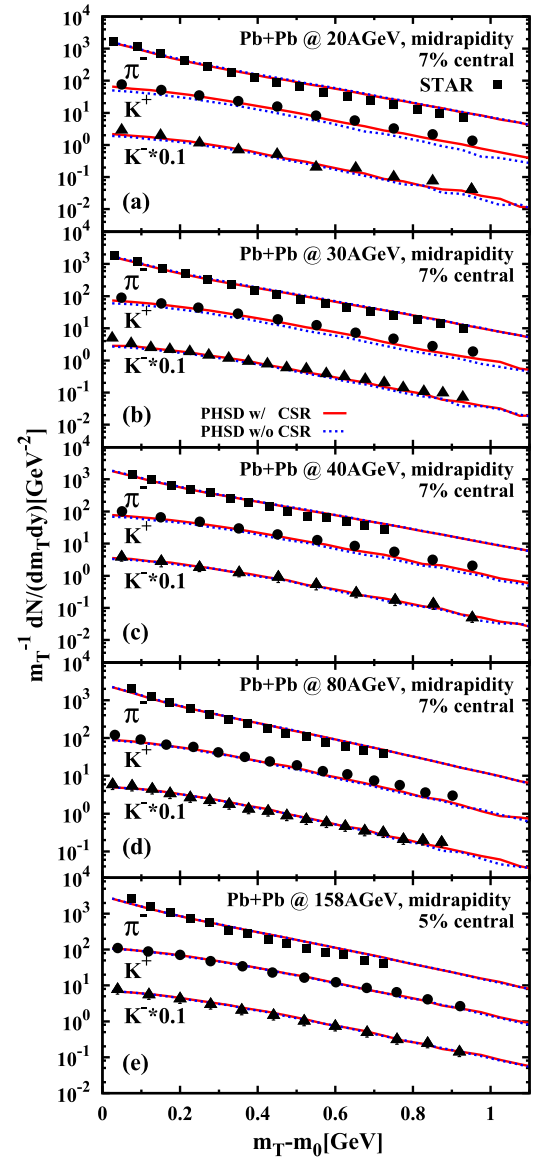

FIG. 12. The transverse mass spectra of pions and kaons for 5% and 7% central Pb+Pb collisions at 20, 30, 40, 80, and 158 A GeV in comparison to the experimental data from Refs. [54,57,63]. The coding of the lines is the same as in Fig. 10.

is no appreciable difference between the calculation with and without CSR, since the energy density reached by the system is not high enough to produce a vanishing scalar quark condensate. Instead, in the energy range $E_{\rm Lab} = 4$–40 A GeV, we notice a small difference between the scenarios with and without CSR. As already mentioned, the CSR acts directly on the chemistry and not so much on the dynamics of the Schwinger mechanism; thus the effect of the partial restoration of chiral symmetry is rather small on the transverse mass spectra. The kaon spectra are harder when CSR is included, while the pion spectra remain essentially unchanged. At the higher SPS energies, $E_{\rm Lab} = 80, 158$ A GeV, the dynamics of the system is ruled dominantly by the QGP phase and our calculations do not show any sensitivity on the inclusion of CSR. The agreement of our PHSD calculations with the data in Figs. 10 and 12 is good in all cases studied. Even if the focus of this work is the study of CSR, we point out that additional kaon potentials might modify this picture at low energies. In particular, the attractive potential for K^- in the hadronic phase should improve our calculations at $E_{\rm Lab} = 8$ A GeV, producing a softening of the spectra. We will report on the effect of hadronic potentials in a forthcoming study.

D. Strange particle abundances and ratios

In this subsection we study the excitation function of the particle ratios K^+/π^+, K^-/π^-, and $(\Lambda + \Sigma^0)/\pi$ at midrapidity from 5% central Au+Au collisions. In Fig. 13 we show the calculations for the following three scenarios: the default PHSD without CSR (blue dotted line) and PHSD including CSR with NL3 and NL1 as parameter sets for the nuclear EoS from the nonlinear σ-ω model (red solid and green dashed lines, respectively). The shaded area displays the uncertainties of our calculations from the two scenarios for the nuclear EoS since the results from the parameter set NL2 are always in between those from NL1 and NL3 (cf. Table II). As already described in Ref. [11], the inclusion of CSR in PHSD is responsible for the strong strangeness enhancement at AGS and low SPS energies. The experimental observations of the ratios K^+/π^+ and $(\Lambda + \Sigma^0)/\pi$ show the well-known horn structure, which is reproduced by the PHSD calculations with CSR. In fact, CSR gives rise to a steep increase of these ratios at energies lower than $\sqrt{s_{NN}} \approx 7$ GeV, while the drop at larger energies is associated to the appearance of a deconfined partonic medium. As anticipated by the considerations in

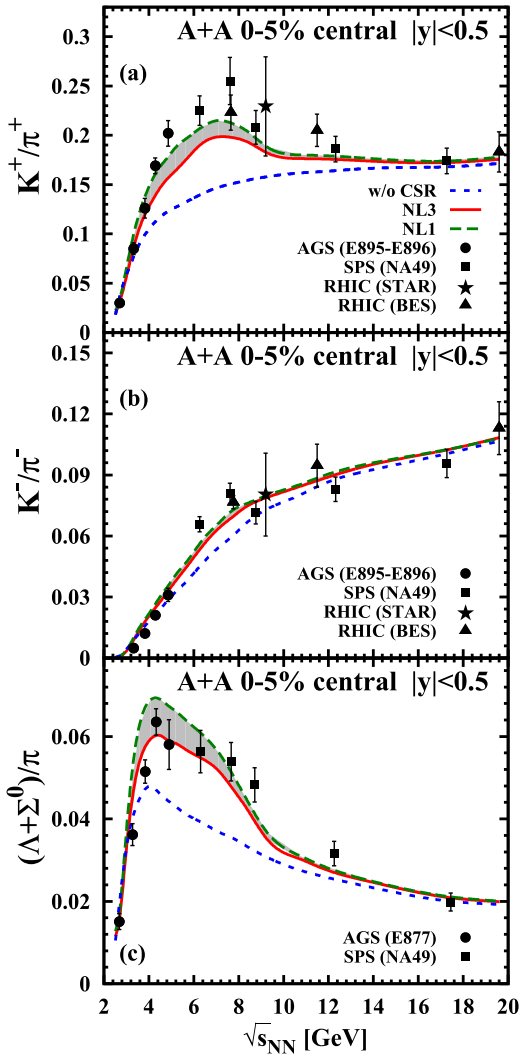

FIG. 13. The ratios K^+/π^+, K^-/π^-, and $(\Lambda + \Sigma^0)/\pi$ at midrapidity from 5% central Au+Au collisions as a function of the invariant energy $\sqrt{s_{NN}}$ up to the top SPS energy in comparison to the experimental data from Refs. [56,61,64]. The coding of the lines is the same as in Fig. 8. The gray-shaded area represents the results from PHSD including CSR, taking into account the uncertainty from the parameters of the σ-ω model for the EoS.

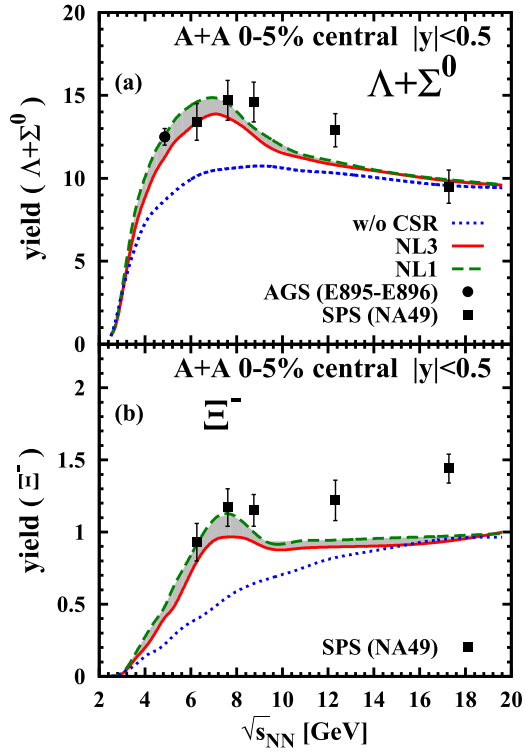

FIG. 14. The yields of $(\Lambda + \Sigma^0)$ and Ξ^- at midrapidity from 5% central Au+Au collisions as a function of the invariant energy $\sqrt{s_{NN}}$ up to the top SPS energy in comparison to the experimental data from Refs. [53,56]. The coding of the lines is the same as in Fig. 13.

Sec. III C, the NL1 parameter set produces a sharper peak both in the K^+/π^+ and in the $(\Lambda + \Sigma^0)/\pi$ excitation functions with a ≈10% maximum increase with respect to the NL3 result that had been reported in Ref. [11]. We point out that even when adopting different parametrizations for the σ-ω model, we recover the same horn feature. This supports the reliability of the CSR mechanism as implemented in the PHSD model.

At AGS energies, the energy dependencies of the ratios K^+/π^+ and $(\Lambda + \Sigma^0)/\pi$ are closely connected, since K^+ and Λ (or Σ^0) are mostly produced in pairs due to strangeness conservation. On the other hand, the excitation function of the K^-/π^- ratio does not show any peak, but it smoothly increases as a function of $\sqrt{s_{NN}}$. In fact, especially at AGS energies, the antikaon production differs substantially from the production of K^+ and Λ, which occurs dominantly via string formation. In fact, the antikaons are produced mainly via secondary meson-baryon interactions by flavor exchange and their production is suppressed with respect to the Λ hyperons that carry most of the strange quarks. This is the reason why the inclusion of chiral symmetry restoration provides a substantial enhancement of the K^+/π^+ and $(\Lambda + \Sigma^0)/\pi$ excitation functions and a smaller change on the K^-/π^- ratio. We also notice that there is no sizable difference between the NL1 and NL3 results for the K^-/π^- ratio. At top SPS energies the strangeness is produced predominantly by the hadronization of partonic degrees of freedom; thus our results for all the ratios do not show an appreciable sensitivity to the nuclear EoS and the calculations with and without CSR tend to merge at $\sqrt{s_{NN}} \approx 20$ GeV.

Finally, in Fig. 14 we present the yields of $(\Lambda + \Sigma^0)$ and Ξ^- at midrapidity from 5% central Au+Au collisions as a function of the invariant energy $\sqrt{s_{NN}}$ in comparison to the available data from Refs. [53–56]. We recover a horn structure, similar to that shown in Fig. 13 for the energy dependence of the strange to nonstrange particle ratios. A sensitivity on the nuclear model parametrizations persists at low energy, while in the top SPS energy regime the results corresponding to the different scenarios merge. The comparison with the available data at $\sqrt{s_{NN}} < 8$ GeV supports the validity of the CSR picture, while at larger energies we underestimate the experimental observations. We mention that this discrepancy

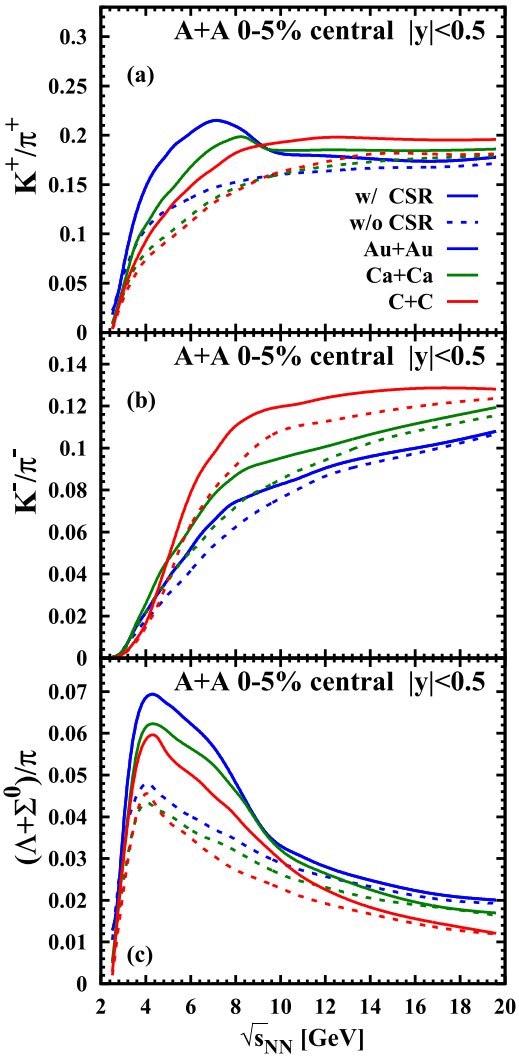

FIG. 15. The ratios K^+/π^+, K^-/π^-, and $(\Lambda + \Sigma^0)/\pi$ at midrapidity from 5% central symmetric $A + A$ collisions as a function of the invariant energy $\sqrt{s_{NN}}$. The solid lines show the results from PHSD including CSR with NL1 parameters; the dashed lines show the result from PHSD without CSR. The blue lines refer to Au+Au collisions, the green lines to Ca+Ca collisions, and the red lines to C+C collisions.

is not due to the CSR mechanism, since it does not play an essential role in the high-energy regime as pointed out above.

V. SYSTEM SIZE AND CENTRALITY DEPENDENCE OF STRANGENESS PRODUCTION

In this section we explore new aspects of CSR in heavy-ion collisions. First, we analyze the dependence of the strange to nonstrange particle ratios on the size of the colliding system (cf. also Ref. [65]). Second, we investigate the effects of CSR on the strange particle yields for different centralities of Au+Au collision. In Fig. 15 we present the particle ratios K^+/π^+, K^-/π^-, and $(\Lambda + \Sigma^0)/\pi$ from PHSD for three types of collision systems. The aim here is to explore how the variation of the system size modifies the excitation functions shown in the previous section. In Fig. 15 we display the calculations for ^{197}Au $+^{197}$Au in blue, for ^{40}Ca $+^{40}$Ca in green, and for ^{12}C $+^{12}$C in red. The scenarios considered are the default PHSD without CSR (dashed lines) and PHSD including CSR with NL1 as parameter set for the nuclear equation of state from the nonlinear σ-ω model (solid lines). The inclusion of CSR gives a strangeness enhancement also in the case of smaller system size with respect to Au+Au collisions and this holds for all three particle ratios. In fact, when considering central collisions, a sizable volume of the system is affected by the partial restoration of chiral symmetry even in case of light ions. We notice that for the K^+/π^+, K^-/π^- ratios, the discrepancy between the calculations with and without CSR remains sizable even at high SPS energies for Ca+Ca and C+C collisions. In particular the spread between the scenarios with and without CSR is larger when the size of the system is smaller. This can be explained by the fact that in Ca+Ca and C+C collisions the fraction of the system which performs the phase transition to the QGP is smaller with respect to Au+Au collisions, and the string excitations and decays still have a large strangeness production rate even at larger energies.

These characteristics are evident also in the observation that at large energies the ratio K^+/π^+ is smaller for the Au+Au collisions and larger in C+C collisions. In fact, we recall that the drop of the K^+/π^+ ratio in Fig. 13 is due to the appearance of the QGP, since the strangeness production in the QGP phase is suppressed with respect to the hadronic production at fixed energy density. Concerning the horn structure in the K^+/π^+ ratio, we notice that the peak of the excitation function becomes less pronounced in the case of Ca+Ca and it disappears completely in the case of C+C collisions. With decreasing system size the low-energy rise of the excitation functions becomes less pronounced. We can see also that the peak for Ca+Ca is shifted to larger energies with respect to the Au+Au case. Unlike K^+/π^+, the $(\Lambda + \Sigma^0)/\pi$ ratio preserves the same structure for all three colliding systems. In order to produce Λ's the threshold energy of $\sqrt{s_{th}} = 2.55$ GeV (for $\Sigma^0\sqrt{s_{th}} = 2.62$ GeV) must be reached, so the $(\Lambda + \Sigma^0)/\pi$ ratio increases when the system easily exceeds this value. The peak of the Λ production is not exactly in correspondence with the threshold energy, since we are considering $A + A$ collisions where the available collision energy is distributed among participants and where secondary and even higher order interactions take place. However, it is interesting to notice that the peak position in this excitation function does not move for different systems, unlike the K^+/π^+ ratios. At large energies the $(\Lambda + \Sigma^0)/\pi$ ratio decreases as a function of the energy, since the pion production is enhanced in the hadronic rescattering. Finally, we observe no peak structure in the energy dependence of the K^-/π^- ratio in any of the scenarios studied. We notice that the results for the different sizes of the system present an opposite hierarchy with respect to the K^+/π^+ and the $(\Lambda + \Sigma^0)/\pi$ ratios. In fact, for C+C and Ca+Ca collisions the pion production is suppressed, since in the small systems the hadronic rescattering cannot develop as in Au+Au collisions.

Furthermore, in Fig. 16 the abundances of pions, kaons, and the most abundant hyperons are plotted as a function

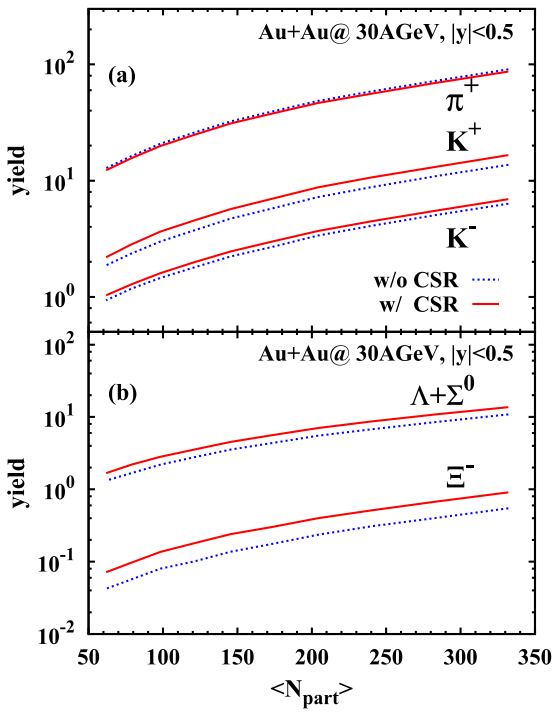

FIG. 16. The particle yields of π^+, K^+, K^-, $\Lambda + \Sigma^0$, and Ξ^- at midrapidity from Au+Au collisions at 30 A GeV as a function of the number of participants. The solid (red) lines show the results from PHSD including CSR with NL3 parameters, and the dotted (blue) lines result from PHSD without CSR.

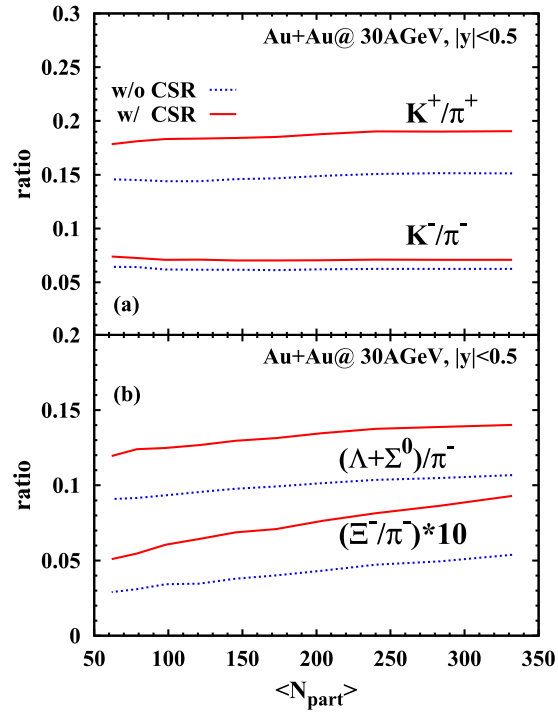

FIG. 17. The particle ratios of K^+/π^+, K^-/π^-, $(\Lambda + \Sigma^0)/\pi^-$, and Ξ^-/π^- (the last one increased by a factor of 10) at midrapidity from 5% central Au+Au collisions at 30 A GeV as a function of the number of participants. The coding of the lines is the same as in Fig. 16.

of the number of participants $\langle N_{\rm part}\rangle$ at midrapidity from Au+Au collisions at 30 A GeV and in Fig. 17 the ratios K^+/π^+, K^-/π^-, $(\Lambda + \Sigma^0)/\pi^-$, and Ξ^-/π^- are shown for the same collision configuration. In both cases we show the calculations from PHSD including CSR with NL3 as parameter set by solid red lines and the calculations from PHSD without CSR by dotted blue lines.

All particle yields decrease with decreasing number of participants. On the other hand, the ratios appear to be almost constant as a function of the centrality for $\langle N_{\rm part}\rangle > 50$. Only the Ξ^-/π^- ratio smoothly decreases with decreasing $\langle N_{\rm part}\rangle$. The inclusion of CSR produces a strangeness enhancement in the whole range of centralities investigated. Note, however, that very peripheral reactions are not considered for $\langle N_{\rm part}\rangle > 50$. At $E_{\rm Lab} = 30$ A GeV the interaction volume of the two colliding nuclei reaches high energy densities such that practically all central cells are influenced by the CSR mechanism independently of the centrality of the collision. Future heavy-ion collision experiments are expected to shed further light on the dynamics of the chiral symmetry restoration by exploring these kind of additional observables.

VI. THERMODYNAMICAL ASPECTS OF STRANGENESS PRODUCTION IN CENTRAL HIC

The aim of this section is to study which parts of the phase diagram in the (T, μ_B) plane are probed by heavy-ion collisions with special focus on the strangeness production. In general it is not straightforward (or even impossible) to connect nonequilibrium dynamics from microscopic transport studies to macroscopic equilibrium properties like temperature and chemical potentials. For this purpose one needs the exact QCD equation of state that relates the energy and the conserved charges to temperature and the chemical potentials of an equilibrated system. As long as lattice calculations at finite chemical potential are prevented by the sign problem one has to rely on effective models, making a study of the phase diagram model dependent. Another issue is what happens if the system reaches local equilibrium during the heavy-ion collision. A common method to decide on kinetic equilibration is the pressure equilibration of the energy momentum tensor $T^{\mu\nu}$. In the local rest frame it takes the form

$$T^{\mu\nu} = \begin{pmatrix} \epsilon & 0 & 0 & 0 \\ 0 & P_x & 0 & 0 \\ 0 & 0 & P_y & 0 \\ 0 & 0 & 0 & P_z \end{pmatrix}, \tag{15}$$

where ϵ is the energy density and P_x, P_y, and P_z are the pressure components in x, y, and z directions. In the center of the collision they are often labeled as $P_x = P_y = P_\perp$ and $P_z = P_\parallel$, when the beam is in the z direction. Due to the initial asymmetry of the collision the longitudinal and the transverse pressure differ significantly. A necessary requirement for kinetic equilibrium is the coincidence of the pressure components $P_\perp \approx P_\parallel$. The behavior of the pressure components in the central region of the collision zone has been

studied in Ref. [66] with the UrQMD transport model [67,68]. It was found that the pressure equilibrates at $t \cong 10$ fm/c after the initial impact of central Au+Au collisions at AGS energies. Additionally, a good agreement between the energy spectra of different hadron species with the predictions of statistical models was found at this time. This indicates that one can indeed find an equilibrated system at AGS energies for times larger than ~10 fm/c.

To fix points in the (T,μ_B) plane we have to determine the temperature T and the baryon chemical potential μ_B of the medium in the expanding fireball. This is usually done by comparing the energy density and the conserved charges in the local cell to the corresponding equation of state [69]. For hadronic matter it is common to use a hadron-resonance gas equation of state. However, it is unclear which hadronic resonances should be included in such a model. We will therefore determine a temperature T and a baryon chemical potential μ_B from the energy density and particle density of nucleons and pions, which are directly accessible within our transport simulations. Instead of examining the whole fireball we will focus on local cells where strangeness is produced; these cells may be close to thermal equilibrium (at late times) or out of equilibrium (at early times). The focus on local cells with strangeness production excludes free streaming cells as well as everything that happens after chemical freeze-out. Whenever a new $s\bar{s}$ pair is produced in the hadronic medium we take the nucleon and pion energy densities ϵ_N and ϵ_π and determine the temperature T and the baryon chemical potential μ_B using the expressions for a noninteracting hadron gas (in equilibrium):

$$\rho_\pi = g_\pi \int \frac{d^3p}{(2\pi)^3} \frac{1}{e^{\omega_\pi/T} - 1}, \tag{16}$$

$$\epsilon_\pi = g_\pi \int \frac{d^3p}{(2\pi)^3} \frac{\omega_\pi}{e^{\omega_\pi/T} - 1}, \tag{17}$$

$$\rho_N = g_N \int \frac{d^3p}{(2\pi)^3} \frac{1}{e^{(\omega_N-\mu_B)/T} + 1}, \tag{18}$$

$$\epsilon_N = g_N \int \frac{d^3p}{(2\pi)^3} \frac{\omega_N}{e^{(\omega_N-\mu_B)/T} + 1}, \tag{19}$$

where $\omega_i = \sqrt{\mathbf{p}^2 + m_i^2}$ is the energy of the respective particle and $g_\pi = 3$ and $g_N = 4$ are the degeneracy factors of pions and nucleons. By additionally evaluating the densities ρ_π and ρ_N we can check if the local cell is in approximate thermal equilibrium or not. In practical terms, if the temperatures obtained from both methods differ by more than 5 MeV or if the chemical potentials differ by more than 15 MeV we consider the cell to be out of equilibrium. Within this procedure we can eliminate further cells from the phase diagram, which are out of equilibrium; however, it does not change the probed area if one considers only events that happen 10 fm/c after the collision.

Figure 18 shows the reconstructed temperatures and chemical potentials for a Au+Au collision at 10.7 A GeV with an impact parameter $b = 2.2$ fm. This reaction is clearly dominated by local cells with partonic content since hadrons in QGP cells dissolve since the energy density is above critical. Each point in Fig. 18 stands for a local cell in which new strange quarks where produced. The color of the points indicates the time of the production (red points early, yellow and green points at intermediate times, blue points at the end of the time interval). Figure 18(a) shows the events from 5 to 7 fm/c after the initial collision. These points cover all chemical potentials up to $\mu_B = 750$ MeV. The maximum temperature is $T = 200$ MeV when adopting only baryons and pions as degrees of freedom. These cells in Fig. 18(a) are dominantly out of thermodynamic equilibrium and for low μ_B and high T correspond to partonic cells with some pion content. Figure 18(b) shows the events from 7 to 10 fm/c where the majority of the points are located at baryon chemical potentials larger than $\mu_B = 150$ MeV. The blue points in Fig. 18(b) belong to cells that are already in equilibrium. Figure 18(c) shows the events that happen at times $t > 10$ fm/c after the initial collision and are approximately in equilibrium. They cover an area between 150 MeV $< \mu_B <$ 650 MeV and 100 MeV $< T <$ 175 MeV. Figure 18(c)

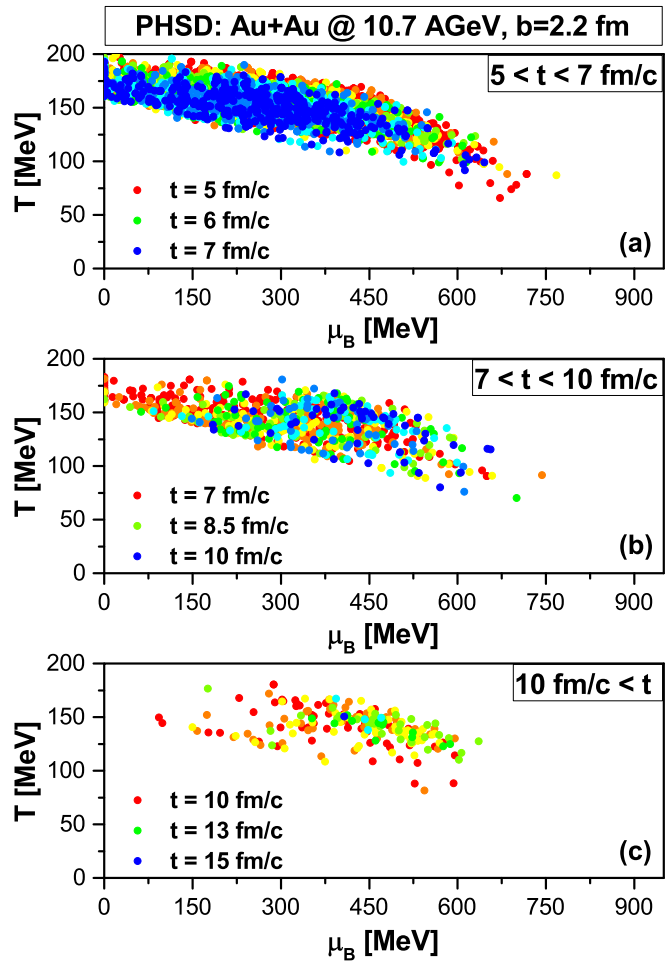

FIG. 18. Occupancy of the phase diagram for hadronic matter in a central Au+Au collision at 10.7 A GeV for different time intervals. Each point belongs to a cell where strange quarks were produced. The color of the points indicates the time of the events within some varying interval. For times >10 fm/c the strangeness production occurs in cells that are in approximate thermodynamic equilibrium while the cells in panels (a) and (b) are dominantly out of equilibrium.

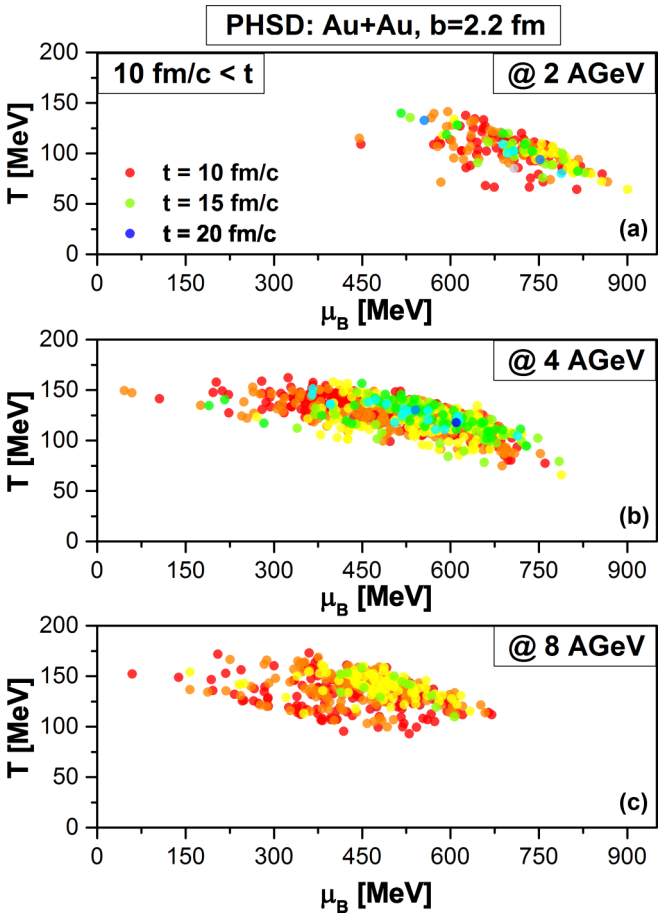

FIG. 19. Occupancy of the phase diagram for hadronic matter in Au+Au collisions at different beam energies from 2 to 8 A GeV for times $t > 10$ fm/c. Each point belongs to a cell where strange quarks were produced. The color of the points indicates the time of the events within some varying interval.

describes indeed a proper phase diagram while Figs. 18(a) and 18(b) suffer from nonequilibrium effects. We stress again that the temperatures and baryon chemical potentials that are shown in Figs. 18(a) and 18(b) cannot be related to any equilibrium properties. In spite of the restrictions imposed by thermodynamic equilibrium we find that even central Au+Au collisions at 10.7 A GeV explore a wide range of points in the T,μ_B plane for μ_B essentially below 650 MeV.

Figure 19, furthermore, shows the occupation of the phase diagram extracted from Au+Au collisions at 2 [Fig. 19(a)], 4 [Fig. 19(b)], and 8 A GeV [Fig. 19(c)] with an impact parameter $b = 2.2$ fm. All points belong to events that happened at times $t > 10$ fm/c after the initial collision. One sees that the probed region shifts to larger baryon chemical potentials and smaller temperatures when lowering the beam energy. The maximum baryon chemical potential in these plots is $\mu_B = 900$ MeV and the lowest temperature is $T = 65$ MeV, however, with a very large spread in T and μ_B.

It is important to discuss how these occupancies in the phase diagram relate to the real QCD phase diagram. Due to the model-dependent EoS, the extracted temperatures and chemical potentials do not represent the real ones for QCD. We recall that the PHSD transport approach uses a critical energy density of $\epsilon_c = 0.5\,\mathrm{GeV/fm^3}$ to distinguish between a hadronic and a partonic medium. If the local energy density is above this threshold the hadrons dissolve into quarks. The critical energy density ϵ_c marks the largest energy density a hadronic system can reach in our simulations. When compared to recent lattice results from the Wuppertal-Budapest collaboration [70] at $\mu_B = 0$ this translates to a temperature of around $T \approx 160$ MeV. On the other side the model used to extract the temperature and chemical potential is based on the hadron resonance gas with a reduced number of degrees of freedom. We mention that a hadron resonance gas (HRG), which contains all the hadronic particles included in PHSD, [2] reaches the critical energy density at temperature $T \approx 175$ MeV. This indicates that the temperatures shown in Figs. 18 and 19 are too large compared to full QCD. As a rough guide one should divide the temperatures in these figures by a factor of $\sim$1.1 in order to obtain an estimate closer to full QCD. For the baryon chemical potential we note that the baryon number susceptibilities χ_B of the HRG are smaller than the lattice results [70]. This implies the corresponding baryon densities, in first order given by $n_B \approx \chi_B\,\mu_B$, exceed the HRG densities, thus overestimating the extracted baryon chemical potentials μ_B in comparison to full QCD. Admittedly we cannot give a definite rescaling for finite chemical potentials; nevertheless, the general trend should be the same in the whole T-μ_B plane shifting the probed area to smaller temperatures and chemical potentials. Nevertheless, it becomes apparent from Fig. 19 that it will be very hard to identify a critical point in the (T,μ_B) plane experimentally since the spread in T and μ_B is very large at all bombardment energies of interest.

VII. SUMMARY

In this work we have analyzed the effects of chiral symmetry restoration (CSR) on observables from heavy-ion collisions in the energy range $\sqrt{s_{NN}} = 3$–20 GeV in extension of the earlier study in Ref. [11]. Our results have been obtained within the parton-hadron-string dynamics transport approach [21], where essential aspects of CSR have been incorporated in the Schwinger mechanism for the string decay [11]. Since the PHSD approach includes both hadronic and partonic degrees of freedom and has been tested in a wide energy regime, it represents a powerful tool to study nucleus-nucleus collisions on a microscopic basis. The CSR, as implemented in PHSD, affects only the hadronic particle production and it does not imply modifications in the quark-gluon plasma (QGP) phase. As already found in Ref. [11] the CSR induces an enhancement of the strange quark fraction γ_s produced via the string decay, while there are no sensible changes in the diquark production and accordingly in baryon-antibaryon production. The s/u ratio, as defined by the Schwinger formula (1), increases as a function of the energy density due to CSR and this is reflected in an enhancement of the strange particle abundances

[2]The hadronic particles included in PHSD are the 0^- and 1^- meson octets, the spin-1/2 and spin-3/2 baryon octets, the $N(1440)$ and $N(1535)$ resonances, and the a_1 meson.

with respect to the nonstrange ones. This has been observed explicitly in the particle spectra at AGS and lower SPS energies ($E_{\rm Lab} = 10.7$ to 30 A GeV). On the other hand, at top SPS energies (e.g., $E_{\rm Lab} = 158$ A GeV) the results from PHSD with and without CSR merge, since the dynamics of the system is dominated by the QGP phase where CSR does not play a significant role.

In extension to Ref. [11] we have performed calculations for different nuclear equations of state (NL1, NL2, and NL3) and thus could quantify the uncertainties in the particle yields and ratios (cf. Figs. 6–8, 13, and 14 as well as Table II). Since the sets NL1 and NL2 give a larger scalar nucleon density ρ_s at the same energy density as the set NL3, the horn in the K^+/π^+ is more pronounced and closer to the experimental data. Furthermore, we found that the transverse mass spectra are only slightly modified by the inclusion of the CSR and are practically insensitive to the nuclear EoS. In fact, the CSR mechanism acts predominantly on the chemistry and not on the kinematics of the string decays.

We stress that our PHSD calculations provide a microscopic interpretation of the horn structure in the excitation function of the K^+/π^+ ratio in central Au+Au (or Pb+Pb) collisions. The steep rise of this ratio at AGS energies is associated to CSR, while the drop at higher SPS energies is due to the appearance of the QGP phase in an increasing volume of the interaction region. We have found an analogous energy dependence for the $(\Lambda + \Sigma^0)/\pi$ ratio, while the excitation function of the K^-/π^- ratio does not show any explicit peak. In general, the PHSD results obtained with the inclusion of CSR are in good agreement with the available data for all observables analyzed, while calculations without CSR fail substantially.

In extension to Ref. [11] we have investigated also different sizes of the colliding ions (^{197}Au, ^{40}Ca, and ^{12}C) and computed the strange to nonstrange particle ratios for these configurations with and without CSR. It is found that the horn feature in the K^+/π^+ ratio appears only for larger system sizes, i.e., Au+Au and Ca+Ca, while the horn disappears in the case of C+C collisions. The $(\Lambda + \Sigma^0)/\pi$ excitation function maintains the peak structure as we have observed in case of Au+Au collisions also for smaller sizes of the system. Furthermore, we have analyzed the strange particle abundances in Au+Au collisions at 30 A GeV as a function of the number of participants in the collision. As mentioned above, when including CSR in the PHSD calculations we obtain an increase of the strange particle yields with respect to the results from PHSD without CSR and this feature is valid in the cases of central collisions as well as moderate peripheral collisions. More experimental observations are needed to extract information about the centrality and system size dependence of the CSR.

We have, furthermore, addressed the question of whether the strangeness production in HIC occurs in thermodynamical equilibrium or not and have found that strange particles are produced dominantly at the early stages of the collisions, when the system is not in thermal and chemical equilibrium. At AGS energies only a few percent of the total strangeness production happens in approximate local thermodynamical equilibrium. With decreasing bombardment energy, lower temperatures and higher baryon chemical potentials are reached; however, the spread in T and μ_B is very large such that a search for a critical point in the phase diagram becomes very difficult experimentally.

In conclusion, our microscopic studies support the idea that CSR occurs in hadronic systems with high temperatures and densities before the deconfinement phase transition takes over. We suggest that the strange particle spectra and yields are suitable signatures to study the properties of CSR in HICs in future also as a function of system size and centrality.

ACKNOWLEDGMENTS

The authors acknowledge inspiring discussions with J. Cleymans, M. Gazdzicki, M. Gorenstein, and O. Linnyk and thank the Helmholtz International Center for FAIR (HIC for FAIR), the Helmholtz Graduate School for Hadron and Ion Research (HGS-HIRe), the Helmholtz Research School for Quark Matter Studies in Heavy-Ion Collisions (H-QM), and the Bundesministerium für Bildung und Forschung (BMBF) for support. The computational resources have been provided by the Center for Scientific Computing (CSC) in the framework of the LandesOffensive zur Entwicklung Wissenschaftlich-ökonomischer Exzellenz (LOEWE).

[1] P. Romatschke and U. Romatschke, Phys. Rev. Lett. **99**, 172301 (2007).
[2] J. Rafelski and B. Müller, Phys. Rev. Lett. **48**, 1066 (1982); **56**, 2334 (1986).
[3] R. Stock, J. Phys. G **28**, 1517 (2002).
[4] M. Gazdzicki and M. I. Gorenstein, Acta Phys. Pol. B **30**, 2705 (1999).
[5] J. Cleymans *et al.* (NA49 Collaboration), Phys. Lett. B **615**, 50 (2005).
[6] A. Andronic, P. Braun-Munzinger, and J. Stachel, Nucl. Phys. A **772**, 167 (2006); Phys. Lett. B **673**, 142 (2009).
[7] K. A. Bugaev *et al.*, Europhys. Lett. **104**, 22002 (2013).
[8] J. Geiss, W. Cassing, and C. Greiner, Nucl. Phys. A **644**, 107 (1998).
[9] E. L. Bratkovskaya, M. Bleicher, M. Reiter, S. Soff, H. Stocker, M. van Leeuwen, S. A. Bass, and W. Cassing, Phys. Rev. C **69**, 054907 (2004).
[10] E. L. Bratkovskaya, S. Soff, H. Stöcker, M. van Leeuwen, and W. Cassing, Phys. Rev. Lett. **92**, 032302 (2004).
[11] W. Cassing, A. Palmese, P. Moreau, and E. L. Bratkovskaya, Phys. Rev. C **93**, 014902 (2016).
[12] P. Senger *et al.*, Lect. Notes Phys. **814**, 681 (2011).
[13] C. S. Fischer, J. Luecker, and C. A. Welzbacher, Phys. Rev. D **90**, 034022 (2014).
[14] C. S. Fischer, L. Fister, J. Luecker, and J. M. Pawlowski, Phys. Lett. B **732**, 273 (2014).
[15] G. Eichmann, C. S. Fischer, and C. A. Welzbacher, Phys. Rev. D **93**, 034013 (2016).

[16] T. K. Herbst, J. M. Pawlowski, and B.-J. Schaefer, Phys. Rev. D **88**, 014007 (2013).
[17] L. McLerran and R. D. Pisarski, Nucl. Phys. A **796**, 83 (2007).
[18] Y. Nambu and G. Jona-Lasinio, Phys. Rev. **122**, 345 (1961).
[19] S. P. Klevansky, Rev. Mod. Phys. **64**, 649 (1992).
[20] R. Rapp, Adv. High Energy Phys. **2013**, 148253 (2013); J. Phys. Conf. Ser. **420**, 012017 (2013).
[21] W. Cassing and E. L. Bratkovskaya, Nucl. Phys. A **831**, 215 (2009).
[22] E. L. Bratkovskaya, W. Cassing, V. P. Konchakovski, and O. Linnyk, Nucl. Phys. A **856**, 162 (2011).
[23] O. Linnyk, V. Konchakovski, T. Steinert, W. Cassing, and E. L. Bratkovskaya, Phys. Rev. C **92**, 054914 (2015); **89**, 034908 (2014); **88**, 034904 (2013); **87**, 014905 (2013); **85**, 024910 (2012); **84**, 054917 (2011); Nucl. Phys. A **855**, 273 (2011).
[24] V. P. Konchakovski, E. L. Bratkovskaya, W. Cassing, V. D. Toneev, S. A. Voloshin, and V. Voronyuk, Phys. Rev. C **85**, 044922 (2012); **85**, 011902 (2012).
[25] L. P. Kadanoff and G. Baym, *Quantum Statistical Mechanics* (Benjamin, New York, 1962).
[26] W. Cassing, Eur. Phys. J. ST **168**, 3 (2009); V. P. Konchakovski, E. L. Bratkovskaya, W. Cassing, V. D. Toneev, S. A. Voloshin, and V. Voronyuk, Nucl. Phys. A **795**, 70 (2007).
[27] O. Linnyk, E. Bratkovskaya, and W. Cassing, Prog. Part. Nucl. Phys **87**, 50 (2016).
[28] B. Nilsson-Almqvist and E. Stenlund, Comput. Phys. Commun. **43**, 387 (1987); B. Andersson, G. Gustafson, and H. Pi, Z. Phys. C **57**, 485 (1993).
[29] T. Sjostrand, S. Mrenna, and P. Z. Skands, J. High Energy Phys. 05 (2006) 026.
[30] W. Cassing and E. L. Bratkovskaya, Phys. Rep. **308**, 65 (1999).
[31] J. Schwinger, Phys. Rev. **82**, 664 (1951).
[32] T. D. Cohen, R. J. Furnstahl, and D. K. Griegel, Phys. Rev. C **45**, 1881 (1992).
[33] U. Vogl and W. Weise, Prog. Part. Nucl. Phys. **27**, 195 (1991).
[34] M. C. Birse, J. Phys. G **20**, 1537 (1994).
[35] V. Koch, Int. J. Mod. Phys. E **06**, 203 (1997).
[36] J. V. Steele, H. Yamagishi, and I. Zahed, Phys. Lett. B **384**, 255 (1996); Phys. Rev. D **56**, 5605 (1997).
[37] G. E. Brown, Prog. Theor. Phys. **91**, 85 (1987).
[38] G. E. Brown, C. M. Ko, Z. G. Wu, and L. H. Xia, Phys. Rev. C **43**, 1881 (1991).
[39] V. Koch and G. E. Brown, Nucl. Phys. A **560**, 345 (1993).
[40] B. Friman, W. Nörenberg, and V. D. Toneev, Eur. Phys. J. A **3**, 165 (1998).
[41] J. M. Alarcon, J. M. Camalich, and J. A. Oller, Phys. Rev. D **85**, 051503 (2012).
[42] M. Hoferichter, J. Ruiz de Elvira, B. Kubis, and U.-G. Meissner, Phys. Rev. Lett. **115**, 092301 (2015).
[43] G. S. Bali, S. Collins, D. Richtmann, A. Schafer, W. Soldner, and A. Sternbeck (RQCD Collaboration), Phys. Rev. D **93**, 094504 (2016).
[44] Y.-B. Yang *et al.*, Phys. Rev. D **94**, 054503 (2016).
[45] J. Bordes, C. A. Dominguez, P. Moodley, J. Penarrocha, and K. Schlichter, J. High Energy Phys. 10 (2012) 102.
[46] M. Hoferichter, J. Ruiz de Elvira, B. Kubis, and U.-G. Meissner, Phys. Lett. B **760**, 74 (2016).
[47] M. Bando, T. Kugo, and K. Yamawaki, Phys. Rep. **164**, 217 (1988).
[48] T. D. Cohen, R. J. Furnstahl, D. K. Griegel, and X. Jin, Prog. Part. Nucl. Phys. **35**, 221 (1995).
[49] J. Boguta and A. R. Bodmer, Nucl. Phys. A **292**, 413 (1977).
[50] A. Lang *et al.*, Z. Phys. A **340**, 287 (1991).
[51] W. Cassing, Nucl. Phys. A **700**, 618 (2002).
[52] J. Stachel, Nucl. Phys. A **610**, 509C (1996).
[53] S. Albergo *et al.*, Phys. Rev. Lett. **88**, 062301 (2002).
[54] C. Alt *et al.* (NA49 Collaboration), Phys. Rev. C **77**, 024903 (2008).
[55] C. Alt *et al.* (NA49 Collaboration), Phys. Rev. C **73**, 044910 (2006).
[56] C. Alt *et al.* (NA49 Collaboration), Phys. Rev. C **78**, 034918 (2008).
[57] S. V. Afanasiev *et al.* (NA49 Collaboration), Phys. Rev. C **66**, 054902 (2002).
[58] T. Anticic *et al.* (NA49 Collaboration), Phys. Rev. C **83**, 014901 (2011); Phys. Rev. Lett. **93**, 022302 (2004).
[59] J. L. Klay *et al.* (E895 Collaboration), Phys. Rev. Lett. **88**, 102301 (2002).
[60] L. Ahle *et al.* (E866 and E917 Collaboration), Phys. Lett. B **476**, 1 (2000); **490**, 53 (2000); Phys. Rev. C **58**, 3523 (1998).
[61] J. L. Klay *et al.* (E895 Collaboration), Phys. Rev. C **68**, 054905 (2003).
[62] C. Alt *et al.* (NA49 Collaboration), arXiv:nucl-ex/0512033v2.
[63] V. Friese *et al.* (NA49 Collaboration), J. Phys. G: Nucl. Part. Phys. **30**, S119 (2004).
[64] B. I. Abelev *et al.* (STAR Collaboration), Phys. Rev. C **81**, 024911 (2010); M. M. Aggarwal *et al.* (STAR Collaboration), *ibid.* **83**, 024901 (2011).
[65] J. Cleymans, B. Hippolyte, H. Oeschler, K. Redlich, and N. Sharma, arXiv:1603.09553v1.
[66] L. V. Bravina *et al.*, Nucl. Phys. A **661**, 600 (1999).
[67] S. A. Bass *et al.*, Prog. Part. Nucl. Phys. **41**, 255 (1998).
[68] M. Bleicher *et al.*, J. Phys. G **25**, 1859 (1999).
[69] S. Endres, H. van Hees, and M. Bleicher, Phys. Rev. C **93**, 054901 (2016).
[70] S. Borsanyi, Z. Fodor, C. Hoelbling, S. D. Katz, S. Krieg, and K. K. Szabo, Phys. Lett. B **730**, 99 (2014).